

REPORT DOCUMENTATION PAGE			Form Approved OMB NO. 0704-0188	
Public Reporting burden for this collection of information is estimated to average 1 hour per response, including the time for reviewing instructions, searching existing data sources, gathering and maintaining the data needed, and completing and reviewing the collection of information. Send comment regarding this burden estimates or any other aspect of this collection of information, including suggestions for reducing this burden, to Washington Headquarters Services, Directorate for information Operations and Reports, 1215 Jefferson Davis Highway, Suite 1204, Arlington, VA 22202-4302, and to the Office of Management and Budget, Paperwork Reduction Project (0704-0188,) Washington, DC 20503.				
1. AGENCY USE ONLY (Leave Blank)		2. REPORT DATE 2/28/06		3. REPORT TYPE AND DATES COVERED Final Progress Report August 1, 2005 - April 30, 2006
4. TITLE AND SUBTITLE Materials Design Principles for the Dynamic Fracture of Laminar Composite Structures			5. FUNDING NUMBERS contract number W911NF-05-C-0073	
6. AUTHOR(S) Brian N. Cox				
7. PERFORMING ORGANIZATION NAME(S) AND ADDRESS(ES) Rockwell Scientific Co. LLC 1049 Camino Dos Rios Thousand Oaks, CA 91360			8. PERFORMING ORGANIZATION REPORT NUMBER PR71267-01	
9. SPONSORING / MONITORING AGENCY NAME(S) AND ADDRESS(ES) U. S. Army Research Office P.O. Box 12211 Research Triangle Park, NC 27709-2211			10. SPONSORING / MONITORING AGENCY REPORT NUMBER 4 8 4 1 4 . 1 - M S	
11. SUPPLEMENTARY NOTES The views, opinions and/or findings contained in this report are those of the author(s) and should not be construed as an official Department of the Army position, policy or decision, unless so designated by other documentation.				
12 a. DISTRIBUTION / AVAILABILITY STATEMENT Approved for public release; distribution unlimited.			12 b. DISTRIBUTION CODE .	
13. ABSTRACT (Maximum 200 words) The goal of this program of basic research is to develop engineering principles for dealing with dynamic, multiple cracking damage in laminated structures, including large scale crack bridging, due to through-thickness reinforcement, and friction. Bridging and friction are treated by materials models at the smallest scales relevant to the mechanisms. By reference to the fundamentals of the dynamic growth of single cracks, which is already largely understood, simple approaches are being formulated to calculate the development of distributed delamination cracks in laminated structures with non-trivial geometry and general loading conditions. To treat large scale bridging effects, structural sub-component models must support dimensions of ~ 100 mm or more. The approach bridges scales ranging from this characteristic structural size down to that of micromechanisms (friction, fiber bridging) within the process zone of a single crack. By doing this, a direct link is being established between structural performance and materials design.				
14. SUBJECT TERMS dynamic delamination, fracture, composites, stitching, z-pinning			15. NUMBER OF PAGES	
			16. PRICE CODE	
17. SECURITY CLASSIFICATION OR REPORT UNCLASSIFIED	18. SECURITY CLASSIFICATION ON THIS PAGE UNCLASSIFIED	19. SECURITY CLASSIFICATION OF ABSTRACT UNCLASSIFIED	20. LIMITATION OF ABSTRACT UL	

Materials Design Principles for the Dynamic Fracture of Laminar Composite Structures

Final Progress Report for the Period August 15, 2005 – February 28, 2006

1. Foreword

Crack bridging (e.g., from stitches or pins) and friction have profound and potentially very useful effects on delamination crack growth, controlling growth rates (damage levels) and the energy absorbed. However, the implications for structural design principles remain quite obscure. The difficulty is that no simple analogue of crack toughness, which underpins static structural design, exists for dynamic cases with large scale bridging effects. The external shape of the structure and the loading configuration dictate stress waves, frictional contact zones, and crack tip stress intensity factors in a way that is very difficult to approach, other than by brute, case specific numerical simulation. The problem is compounded by the reality of multiple cracking, a complexity that is rarely entertained in laboratory fracture specimen design. Physically sound materials models for the important structural problem of multiple, nonlinear cracking in laminated structures with large-scale bridging due to friction and reinforcement remain, in spite of the technological importance of these systems, undeveloped.

We are conducting a program of basic research to develop engineering principles for dealing with dynamic, multiple cracking damage in laminated structures, including large scale crack bridging, due to through-thickness reinforcement, and friction. Bridging and friction will be treated by materials models at the smallest scales relevant to the mechanisms. By reference to the fundamentals of the dynamic growth of single cracks, which is already largely understood (although some interesting mysteries remain), simple approaches will be formulated to calculating the development of distributed delamination cracks in laminated structures with non-trivial geometry and general loading conditions. To treat large scale bridging effects, structural sub-component models must support dimensions of ~ 100 mm or more. Our approach must bridge scales ranging from this characteristic size down to that of micromechanisms (friction, fiber bridging) within the process zone of a single crack. By doing this, a direct link will be established between structural performance and materials design.

Our research aims to create a systematic method for simplified design of laminated engineering structures, which will impact the design and performance of all lightweight military vehicles and structures. Newly gained understanding will point to significant improvements in impact and ballistic resistance via materials and structural design.

The program is being conducted with formal collaborations with universities in the U.S. and Italy, with arrangements pending with universities in Australia and Denmark. All these collaborations involve Ph.D. candidate students, including extended stays for students at Rockwell Scientific.

2. Table of Contents

1.	Foreword	1
2.	Table of Contents	2
3.	List of Appendices, Illustrations, and Tables	3
4.	Statement of the Problem Studied	4
5.	Summary of the Most Important Results	5
6.	List of all Publications Supported under this Contract	10
7.	List of all Participating Personnel	11
8.	Report of Inventions	12
9.	Bibliography	13
10.	Appendices	14

3. List of Appendices, Illustrations, and Tables

Appendices – reprints of two journal papers:

Andrews, M.G., Massabò, R., Cox, B.N., 2006. Elastic interaction of multiple delaminations in plates subject to cylindrical bending. *International Journal of Solids and Structures* 43, 855-886

Yang, Q.D., Rosakis, A.J., Cox, B.N., 2006. Dynamic fiber sliding along debonded, frictional interfaces. *Proceedings of the Royal Society* in press

Illustrations:

Figure 1. (a) X-ray image of delamination crack growing from the tip of a sharp notch (Spearing and Beaumont, 1992). (b) Prediction in which delamination and splitting cracks are the only damage. (c) Prediction in which delamination and splitting cracks are accompanied by distributed softening (due to microcracking) in the laminate plies.

Figure 2. Normalized energy release rate of a single centrally located stationary crack in a clamped beam specimen, with first natural period T_1 subject to different pulse durations, T_p .

Tables:

none

4. Statement of the Problem Studied

In this three-year program of basic research we shall:

- (i) formulate and solve multiple delamination problems, by methods applicable to reasonably complex structures and loading, that correctly describe fundamental aspects of dynamic delamination crack growth in the presence of large scale bridging and friction;
- (ii) establish engineering principles for modeling and designing laminated structures with energy absorption optimized by tailoring crack bridging and friction mechanisms.

The main thrust of our work will be theoretical. Use will be made where possible of data in the literature.

Our objectives are to:

Conduct basic research into the development of distributed dynamic delamination cracks in laminated structures with non-trivial geometry and general loading conditions and in the presence of friction and bridging due to through-thickness reinforcement such as stitches or rods.

Develop engineering principles for dynamic, multiple cracking damage in laminated structures, including large scale crack bridging and friction.

Create a systematic method for simplified design of laminated engineering structures containing through-thickness reinforcement, which will shorten the design cycle for all lightweight military vehicles and structures.

Indicate means for achieving significant improvements in impact and ballistic resistance via materials and structural design, especially via manipulation of friction or the bridging effects of through-thickness reinforcement.

5. Summary of the Most Important Results

Our objective in the first year is to formulate multiple delamination problems in a number of cases that will be widely representative of common structural applications. Formulations are sought, using approximations where they are valid and helpful, that decouple extrinsic, shape and load dependent factors from the intrinsic nonlinear material response of the damaged laminate. Large scale bridging conditions of friction and through-thickness reinforcement will be included.

Three modeling approaches are of possible interest, viz., 1) beam or plate level approximations; 2) weight function methods; and 3) computational methods. In the first year, selected problems will be solved in the static limit, building on our prior related work (Andrews *et al.*, 2006; Yang and Cox, 2005). Dynamic solutions are also being formulated and solved.

Mixed Mode Cohesive Models – Interacting Failure Mechanisms

In work performed under other programs, Qingda Yang and Brian Cox have formulated high fidelity simulations of multiple delamination events under static loading in laminated composites, using cohesive zone representations of the nonlinear processes associated with material failure in the crack tip region. While a vast and long literature exists on delamination mechanics (see our full review in the Introduction to (Yang and Cox, 2005)), our work presents important new advances that make a big difference to whether the outcome will be truly high in fidelity. In our new ARO program, we have extended our formulation to include multiple mechanisms of damage and shown that the interaction between different mechanisms can dominate damage evolution.

Key points we have contributed, including prior work, which we list here for completeness in presenting our point of view, and work done in our new program, are as follows.

1. Cohesive models of dominant cracks give a physically consistent description of damage initiation (requiring no assumed initial defect), the progression of damage to a traction-free crack, and the propagation of the crack towards the limit of linear elastic fracture mechanics. All of these stages of crack development are contained in a single, unifying model – the cohesive traction law.
2. Linear elastic fracture mechanics (LEFM), e.g., as embodied in the virtual crack closure technique, is very limited in its ability to generate high fidelity simulations of damage evolution. There remains, in our opinion, no rational method of predicting damage initiation at locations of elastic stress singularity using LEFM; one always runs into the vexed questions of what initial defect might exist and how stress singularities are to be treated computationally. These difficulties are, in principle, completely overcome in a cohesive zone model, which provides a physically valid depiction of nonlinear material behavior prior to crack formation; and introduces a length scale, the cohesive zone length, which plays an essential role in developing physically appropriate, nonsingular stress representations.

3. The initiation of damage and the evolution of the crack are complex processes, involving continuous changes in the shape of the crack and the mode ratio, which varies strongly around the crack front. A high-fidelity simulation must be allowed to predict the crack shape evolution – it cannot be specified *a priori*. Shape and mode ratio characteristics follow as computational results, computed in real time during a simulation, naturally and very easily from a mixed mode cohesive zone representation.

4. The cohesive zone has a characteristic length that can be predicted *a priori* using analytical results, which we and our collaborators have previously derived (Cox and Marshall, 1994; Massabò and Cox, 1999). We have now assembled the prior results into simple rules for establishing the maximum computational mesh size for simulations (Yang and Cox, 2005). If the mesh is too coarse (elements larger than the cohesive zone length), mesh-independence cannot be achieved. Almost all prior literature on cohesive zones in delamination based on plate elements (or similar 2D elements) fails to meet this criterion! Fortunately, the progression of computational power makes it feasible to use elements that are properly sized; the motivation for using plate elements is not as compelling as it has been in the past.

5. For components of complex shape (e.g., containing cut-outs), strong through-thickness stresses provide a further reason for avoiding plate elements. Three-dimensional solid finite elements are preferable. Once again, advances in computer power make using solid elements feasible.

5. (New work in this program) The interaction between different damage modes can be very strong. High fidelity simulations require the treatment of dominant delamination cracks, distributed matrix microcracking, and matrix shear damage all at once.

The last point summarized above was demonstrated in some of the first work done in this ARO program. Details are shown in Figure 1. In earlier work of ours in which only delamination and splitting cracks were included as possible failure modes, many of the features of a delamination crack emanating from a sharp slit were qualitatively reproduced, but the exact predicted shape of the delamination crack (Figure 1b) was not the same as seen experimentally (Figure 1a). When a continuum damage representation of ply softening was included along with interlaminar and splitting cracks, the agreement with experiment became excellent (compare Figures 1a and 1c). These results, we believe, strongly encourage the prospect of high fidelity simulations of damage using recent physical formulations of damage and current computer power.

One of our objectives in the new program is to develop similar simulations to those depicted in Fig. 1 in the dynamic regime.

Beam Theory Solutions for Multiple Delamination

As well as numerical formulations, we have continued a prior line of research (Andrews *et al.*, 2004; Andrews *et al.*, 2005; Andrews *et al.*, 2006; Cox *et al.*, 2004) into the applicability of advanced beam theory methods. This effort has proven a good investment, since, in many cases of interest, beam theory is surprisingly accurate when appropriately formulated and has given insight into deformations and energy release rates associated with multiple delamination cracking that may not have been nearly as clearly

highlighted by purely numerical work.

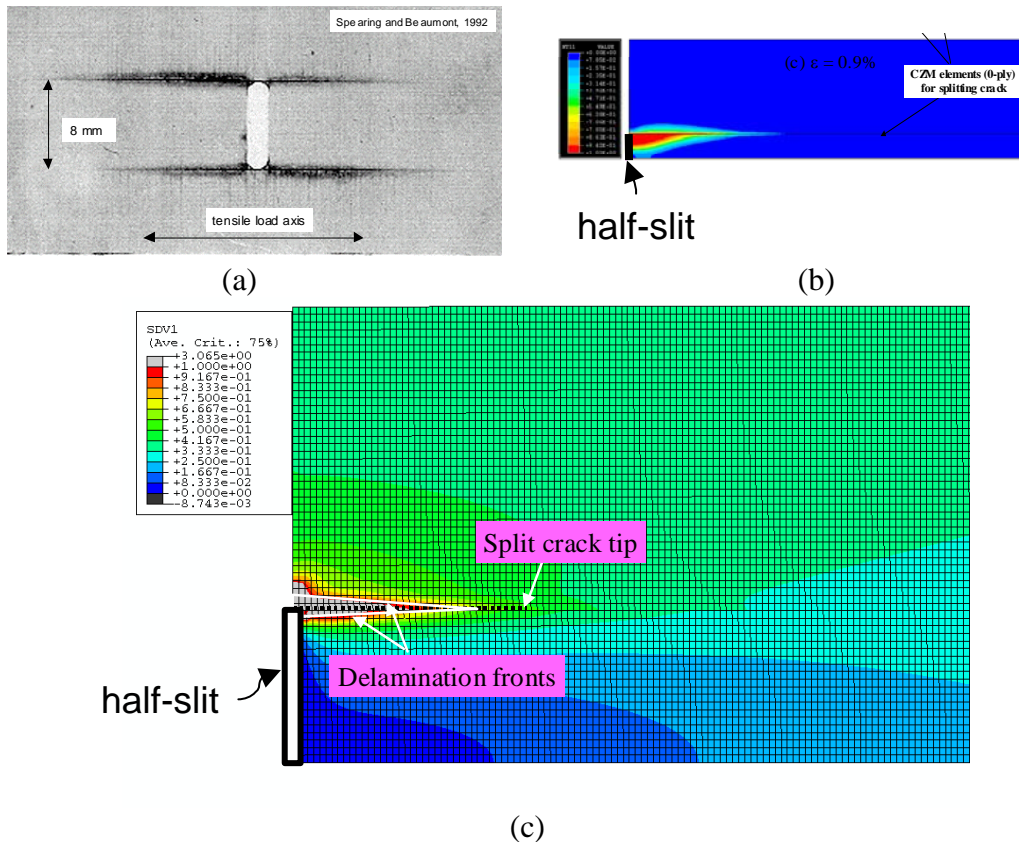


Figure 1. (a) X-ray image of delamination crack growing from the tip of a sharp notch (Spearing and Beaumont, 1992). (b) Prediction in which delamination and splitting cracks are the only damage. (c) Prediction in which delamination and splitting cracks are accompanied by distributed softening (due to microcracking) in the laminate plies.

A model was formulated for the multiple delamination of orthotropic plates subject to static and dynamic loading and deforming in cylindrical bending (Andrews and Massabò, 2005). The model was based on a particularization of Timoshenko beam theory and accounts for cohesive and bridging mechanisms as well as contact and friction acting along the delamination surfaces. The model also accounts for the local elastic deformation at the delamination tips, which give rise to relative rotations between the different sub-beams (root rotations), through rotational springs. The springs are activated by the crack tip stress resultants, normal and shear forces and bending moments. The compliances of the springs have been derived numerically for a wide range of elastic constants. Accounting for the root rotations substantially improves the accuracy of the one-dimensional model, leading to results that are in excellent agreement with rigorous two-dimensional solutions. In addition, it allows for closed form derivation of analytical expressions for the energy release rate and stress intensity factors. These expressions are an extension of work by Suo *et al.* and Li *et al.* to account for shear, near tip deformation and multiple delaminations. They depend only on the crack tip stress resultants, the

elastic constants, the geometry and the compliances of the springs describing the root rotations. These analytical results are, we feel, an important contribution to the fundamental development of beam theory for fracture studies.

The model has been used to re-examine single delamination specimens of standard fracture tests. The validity of the model has also been demonstrated in multiple delamination systems, where mixed mode conditions often occur, and for orthotropic materials with a large mismatch in elastic parameters, for which simplified models neglecting root rotations yield inaccurate predictions. The limitations of the model, as well as of all models based on a first order approximation of shear, in dealing with short process zone lengths at the delamination tip where cohesive tractions act parallel to the delamination surfaces have been highlighted. These limitations can be removed using higher order theories.

The model has been applied to investigate the interaction effects of multiple delaminations and of delaminations and regions of small delamination damage. Phenomena of amplification and shielding of the energy release rate and modifications in the mode ratio have been observed. The different regimes of behavior have been defined for a system of two delaminations in a cantilever beam.

Finally, in a phase of the work that is essential for the current program, the model has been used to investigate the effect of different dynamic loading pulse durations on the fracture parameters of delaminated plates. Regimes of amplification and shielding of the energy release rate due to dynamic effects have been identified for a clamped beam with a single delamination (Fig. 2) and the results have been summarized using shock spectra. These first results for dynamic delamination will be used in our future work, including numerical simulations, as standards for limiting cases.

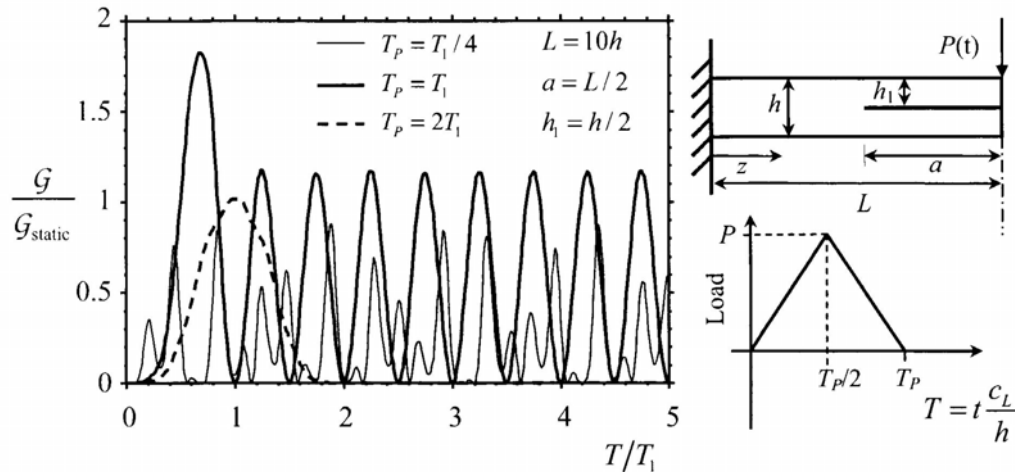


Figure 2. Normalized energy release rate of a single centrally located stationary crack in a clamped beam specimen, with first natural period T_1 subject to different pulse durations, T_p .

The question of whether a numerical approach or beam theory is most appropriate for our further studies is central in our minds. As we move into problems with more complicated material effects, such as stitching and crack face friction, as well as specimens or

components with non-trivial geometry, numerical methods will obviously be favoured. However, beam theory results continue to prove valuable for analyzing limiting cases, for the special insight they can yield into the chief factors governing structural response.

Dynamic Fiber Sliding

In a collaboration with Professor Ares Rosakis of California Institute of Technology, we completed a detailed study of the physics of interfacial sliding in the prototypical problem of a fiber being pulled dynamically out of a matrix (Yang *et al.*, 2006). This work was initiated under a prior ARO grant (DAAD19-99-C-0042). A substantial amount of work on the problem and the writing of the resulting paper were then performed without funding, after that grant had expired. Under the new grant covered by this report (W911NF-05-C-0073), revisions were then performed in August and September, 2005, in response to some interesting ideas raised by the journal reviewers. The original contributions of the paper include: details of the deformation mechanics of the dynamic pullout problem; confirmation using numerical results of the accuracy of simple analytical shear lag solutions (detailed by us elsewhere (Sridhar *et al.*, 2003)); and the interesting observation, in experiments and simulations, of indications of complex deformation, perhaps involving chaotic behaviour, during unloading. The contributions contained specifically in the revisions made under this contract relate to the inference of information about interfacial friction from our experiments, using the analysis of our numerical simulations. We point out especially that the disorder found upon unloading is insensitive to details of the friction law, which raises an essential distinction vis-a-vis ill-posedness and instability remarked previously in the literature, which depend on the friction quite sensitively. Furthermore, whereas all prior studies considered time-uniform far-field loading rates, our observations show disorder confined to the unloading regime – the loading regime is smoothly behaved. The possibility that unloading creates qualitative effects in deformation fields that are not observed for rising or uniform loading is therefore raised.

6. List of all Publications Supported under this Contract

(a) Papers published in peer-reviewed journals

Andrews, M.G., Massabò, R., Cox, B.N., 2006. Elastic interaction of multiple delaminations in plates subject to cylindrical bending. *International Journal of Solids and Structures* 43, 855-886

Yang, Q.D., Rosakis, A.J., Cox, B.N., 2006. Dynamic fiber sliding along debonded, frictional interfaces. *Proceedings of the Royal Society* in press

(b) Papers published in non-peer-reviewed journals or conference proceedings

none

(c) Papers presented at meetings but not published

none

(d) Manuscripts submitted, not published

Andrews, M.G., Massabò, R., 2005. The role of local tip deformation on mixed mode delamination. *International Journal of Fracture* submitted..

(e) Technical reports submitted to ARO

none

7. List of all Participating Personnel

Dr. Qingda Yang, Member of Technical Staff, Rockwell Scientific Co. LLC

Dr. Brian Cox, Principal Scientist, Rockwell Scientific Co. LLC and Adjunct Professor, Sydney University, Sydney, Australia

Professor Roberta Massabò, University of Genova, Genova, Italy and Adjunct Professor, Northwestern University, Chicago, Illinois

Dr. Martin Andrews, Ph. D. candidate, Northwestern University (supervisor, Professor Roberta Massabo).*

Mr. Farrock Fazileh, Ph. D. candidate, University of Genova, Genova, Italy.

Mr. Weixing Josh Zhou, Ph. D. candidate, University of Illinois at Urbana Champaign (supervisor, Professor Yonggang Young Huang).**

*Dr. Andrews earned a Ph. D. (Northwestern University) partly while supported by this contract.

**Mr. Zhou is currently on a six-month assignment, which began January 1, 2006, at Rockwell Scientific Co. LLC, in our Thousand Oaks facility, under the supervision of Drs. Qingda Yang and Brian Cox.

Arrangements are being made for Mr. Christian Lundsgaard-Larsen to visit Rockwell Scientific Co. LLC, Thousand Oaks facility, for a 3 – 5 month stay, to work under the supervision of Drs. Qingda Yang and Brian Cox. Mr. Lundsgaard-Larsen is a Ph. D. candidate at the Technical University of Denmark (DTU), supervised by Professors Jorgen Jensen, Christian Berggreen, and Bent Sorenson.

A proposal is being written with Professors Yiu-Wing Mai and Lin Ye at the University of Sydney, where Brian Cox is an Adjunct Professor, to fund dynamic delamination experiments. While this proposal would bring no funding to Rockwell Scientific, it would enable collaborative work involving students at the University of Sydney, with technical exchange facilitated by visits to Australia and Rockwell Scientific.

8. Report of Inventions

There have been no inventions in this contract to date.

9. Bibliography

Andrews, M.G., Massabò, R., Cox, B.N., 2004. Multiple delamination of laminated structures. 17th National Conference of Italian Group of Fracture, June, 2004, Bologna: Gruppo Italiano Frattura.

Andrews, M.G., Massabò, R., 2005. The role of local tip deformation on mixed mode delamination. *International Journal of Fracture* submitted.

Andrews, M.G., Massabò, R., Cox, B.N., 2005. Multiple delamination of delaminated structures. *International Conference on Fracture, ICF 11*, March, 2005, Torino, Italy.

Andrews, M.G., Massabò, R., Cox, B.N., 2006. Elastic interaction of multiple delaminations in plates subject to cylindrical bending. *International Journal of Solids and Structures* 43, 855-886.

Cox, B.N., Marshall, D.B., 1994. Concepts for bridged cracks in fracture and fatigue. *Acta Metallurgica et Materialia* 42(2), 341-363.

Cox, B.N., Andrews, M.G., Massabò, R., Rosakis, A.J., Sridhar, N., Yang, Q.D., 2004. Shear lag and beam theories for structures. *Structural Integrity and Fracture Conference*, September, 2004, Brisbane, Australia: Australian Fracture Group Inc.

Massabò, R., Cox, B.N., 1999. Concepts for bridged mode II delamination cracks. *Journal of the Mechanics and Physics of Solids* 47, 1265-1300.

Spearing, S.M., Beaumont, P.W.R., 1992. Fatigue damage mechanics of composite materials. I: experimental measurement of damage and post-fatigue properties. *Composites Science and Technology* 44, 159-168.

Sridhar, N., Yang, Q.D., Cox, B.N., 2003. Slip, Stick and Reverse Slip Characteristics during Dynamic Fiber Pullout. *Journal of the Mechanics and Physics of Solids* 51(7), 1215-1241.

Yang, Q.D., Cox, B.N., 2005. Cohesive models for damage evolution in laminated composites. *International Journal of Fracture* 133(2), 107-137.

Yang, Q.D., Rosakis, A.J., Cox, B.N., 2006. Dynamic fiber sliding along debonded, frictional interfaces. *Proceedings of the Royal Society* in press.

10. Appendices

Andrews, M.G., Massabò, R., Cox, B.N., 2006. Elastic interaction of multiple delaminations in plates subject to cylindrical bending. *International Journal of Solids and Structures* 43, 855-886

Yang, Q.D., Rosakis, A.J., Cox, B.N., 2006. Dynamic fiber sliding along debonded, frictional interfaces. *Proceedings of the Royal Society* in press

Elastic interaction of multiple delaminations in plates subject to cylindrical bending

Martin G. Andrews^a, Roberta Massabò^{b,*}, Brian N. Cox^c

^a *Department of Civil and Environmental Engineering, Northwestern University, Evanston, IL 60208, USA*

^b *Department of Structural and Geotechnical Engineering, University of Genova, Genova 16145, Italy*

^c *Rockwell Scientific Co., Thousand Oaks, CA 91360, USA*

Received 14 October 2004; received in revised form 8 April 2005

Available online 15 June 2005

Abstract

This paper deals with the elastic interaction of multiple through-width delaminations in laminated plates subject to static out of plane loading and deforming in cylindrical bending. A model has been formulated utilizing the classical theory of the bending of beams and plates and accounting for non-frictional contact along the delamination faces. Strong interaction effects arise between the delaminations including shielding and amplification of the energy release rate and modification of the mode ratio as compared to a structure with only a single delamination. Such behavior has been summarized in maps that completely characterize the response of a system of two delaminations in a cantilever beam. The quasi-static propagation of the system of delaminations is also strongly controlled by the delamination interactions, which lead to local snap-back and snap-through instabilities, crack arrest and crack pull-along. The results show similarity to those for cracked infinite bodies, but the finite-thickness of the plate plays an important role and gives rise to more complex behaviors. The stability of the equality of length of a system of n delaminations is controlled by their spacing. Finite element calculations confirm that the model proposed here is accurate, except when the difference in the length of the interacting delaminations is less than a few times the separation of their planes.

© 2005 Elsevier Ltd. All rights reserved.

Keywords: Multiple delamination; Shielding; Amplification; Crack interaction; Laminated structures

1. Introduction

Due to poor interlaminar properties, laminated fiber reinforced composites are susceptible to delaminations caused for instance by manufacturing errors, edge effects or by such in service situations as impact,

* Corresponding author. Tel.: +39 010 353 2956; fax: +39 010 353 2534.

E-mail address: massabo@diseg.unige.it (R. Massabò).

monotonic and cyclic loading. In the case of impact, typically many delaminations occur between layers of different fiber orientation. The presence of the delaminations is often undetectable on the surface and may significantly reduce the stiffness and load carrying capacity of the structure (Pavier and Clarke, 1995). When a load is applied that causes sufficient interlaminar stresses, the delaminations may grow, often catastrophically, separating the structure into two or more pieces and causing further reduction in stiffness and/or failure. While the behavior of structures in the presence of a single delamination has been widely studied since the early work of Kanninen (1973, 1974) and others (see Massabò and Cox, 1999; Sridhar et al., 2002 for work of the authors), the problem of the multiple delamination of laminated structures is not yet fully understood. This paper examines the interaction of multiple delaminations in plates subject to static out of plane loading and the effects this interaction has on the fracture behavior and structural response of the laminate, using a cantilever plate as a case study.

An important interaction effect is contact that may occur between the delaminated plies. When there are multiple delaminations, studies, such as those dealing with structures subject to in plane loadings (Larsson, 1991; Suemasu, 1993), have shown that extensive contact may occur along the delaminations faces. Contact significantly affects the critical energy release rate for the extension of a delamination. Contact also introduces regions in which friction may be important. The presence of contact will be shown later not to be limited to delaminated structures subject to in-plane loading.

The effect of the interaction of the delaminations on the energy release rates is another important phenomenon. Larsson (1991), using a model based on the theory of bending of plates to study delaminated plates under in-plane loading, observed a discontinuity in the energy release rate of a delamination when its length is equal to the length of other delaminations of the system. This discontinuity was thought to be an anomalous product of the assumptions of plate theory; however, this paper will show that the discontinuity well approximates the actual behavior. Zheng and Sun (1998) showed that the effect of the interactions between delaminations on the energy release rates depends on the through-thickness distance between the delaminations. For the structure and crack configurations that they studied, they also observed that the presence of a smaller delamination has little effect on the energy release rate of a delamination, while the presence of a longer delamination may induce strong amplification or shielding. This paper will show that in more general crack configurations, the presence of short delaminations may also strongly affect the response.

The interaction effects also influence the stability of the equality of length of a system of n delaminations. As it will be shown later, the delaminations of a stable system will tend to grow together, leading to an increased capacity of the system to absorb energy and a more ductile structural response. An unstable system of delaminations will have more localized delamination growth of only one or a small number of delaminations, leading to reduced energy absorption and a less ductile response. Suemasu and Majima (1996) showed that an axisymmetric system of equally spaced, equal size, penny-shaped delaminations in a clamped circular plate subject to a concentrated static force is stable. More general conclusions on the stability of systems of delaminations with unequally spaced cracks will be presented in the following.

The model proposed in this paper is based on the theory of bending of beams and plates and examines a multiply delaminated plate subject to static, out of plane loading and deforming in cylindrical bending. Non-frictional contact along the delamination surfaces is accounted for utilizing three approximations, two of which allow closed form solutions of the problem. The energy release rate and the stress intensity factors at each delamination crack tip are determined by the application of methods developed for beams and plates with a single delamination. The results are quantified for the case of a cantilever beam with multiple edge delaminations. Shielding and amplification of the energy release rates of the cracks and the interaction effects on the macro structural response of the plate are examined. The model is validated through finite element analyses.

2. Theoretical model

2.1. Model assumptions

The problem under consideration is a thin laminated plate of thickness h with n through width delaminations. A system of Cartesian coordinates x – y – z is introduced. Each delamination, with index i , is arbitrarily distributed across the thickness, with through-thickness position y_i and length a_i . The plate is subject to out of plane loading. An exemplary plate, with an applied surface pressure q , is shown in Fig. 1a.

The material comprising the plate is assumed to be homogeneous, isotropic and linear elastic, with elastic modulus E and Poisson's ratio ν . The model is applicable to all laminates composed of isotropic layers of the same material. With modifications to account for different material properties in the through thickness direction, the model can also be applied to quasi-isotropic laminates and specially orthotropic laminates (i.e. laminates composed of layers whose principal material directions are aligned with the reference axes) with a large number of layers.

Only small deformations of the plate are considered, and plane strain conditions are assumed parallel to the x – y plane so that the plate deforms in cylindrical bending. Therefore, the governing equations of the plate correspond to those of a beam with a reduced Young's modulus $\bar{E} = E/(1 - \nu^2)$, where E is the longitudinal modulus. In the following analysis, the designation of beam and plate are identical. The classical theory of bending of beams, which neglects shear deformation, is utilized to determine the response of the delaminated structure.

The plate shown in Fig. 1a, is decomposed into multiple uncracked beam segments, defined by the coordinates of the crack tips and continuity conditions are applied at the cross sections separating beam segments. For purposes of notation, the beam segments are numbered from top to bottom and left to right in the structure, and delaminations are numbered from top to bottom. The height of beam segment k is h_k and its cross sectional moment of inertia and area are I_k and A_k , respectively. The generalized displacements of the centroidal axis of beam segment k are the axial and transverse displacements u_k and w_k , and the bending rotation φ_k . The stress resultants per unit width are axial force N_k , shear force V_k and bending moment M_k (Fig. 1b).

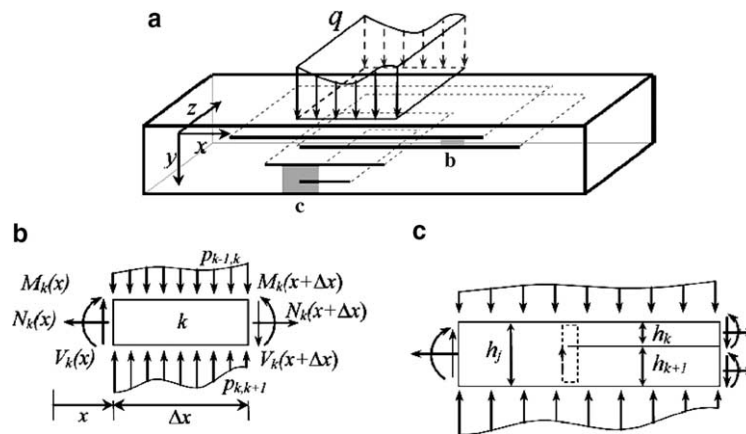


Fig. 1. (a) Exemplary plate with multiple through width cracks subject to transverse loading. (b) Equilibrium of a beam segment, showing stress resultants and contact pressures. (c) Crack tip element separating beam segments identified by j , k and $k + 1$. The dashed line is the path used for calculating the J integral.

Assuming no shear deformation, $\gamma_k = 0$, the compatibility equations for the beam segment k are

$$\varphi_k = -w_{k,x}, \quad \epsilon_k = u_{k,x}, \quad \kappa_k = \varphi_{k,x}, \quad (1)$$

where ϵ_k is the axial deformation and κ_k is the bending curvature and, x denotes differentiation with respect to the longitudinal coordinate x . The constitutive equations are

$$M_k = EI_k \kappa_k = -EI_k w_{k,xx}, \quad N_k = EA_k \epsilon_k = EA_k u_{k,x}, \quad (2)$$

Equilibrium of the beam segment is given by:

$$M_{k,x} - V_k = 0, \quad V_{k,x} + p_{k,k+1} = p_{k-1,k}, \quad N_{k,x} = 0, \quad (3)$$

where $p_{k,k+1}$ and $p_{k-1,k}$ are either externally applied pressures or contact pressures acting on the lower and upper surfaces of the segment (Fig. 1b).

At the i th crack tip, Fig. 1c, with coordinate $x = x_i$ separating the beam segments j , k and $k + 1$, the kinematic and static continuity conditions are

$$\begin{aligned} u_j + \frac{1}{2}(h_j - h_k)w_{j,x} &= u_k, & u_j - \frac{1}{2}(h_j - h_{k+1})w_{j,x} &= u_{k+1}, \\ w_j &= w_k = w_{k+1}, \\ w_{j,x} &= w_{k,x} = w_{k+1,x}, \\ N_j &= N_k + N_{k+1}, \\ M_j &= M_k + M_{k+1} - \frac{1}{2}(h_j - h_k)N_k + \frac{1}{2}(h_j - h_{k+1})N_{k+1}, \\ V_j &= V_k + V_{k+1}. \end{aligned} \quad (4)$$

The bending rotations of the beam segments at the crack tips, often referred to as root rotations, have been assumed in (4) to be identical to one another.

In the plate shown in Fig. 1a, depending on the loading conditions and the geometry of the delamination system, contact along the delamination surfaces may occur. This contact is assumed to be non-frictional, which allows free sliding along the surfaces of a delamination, and is represented by the contact pressures, $p_{k,k+1}$ and $p_{k-1,k}$. The presence of contact is simulated in three ways.

The first method is to assume that the deflections of the beams in the delaminated regions are the same. Interpenetration along the delamination surfaces is then avoided; however, the beam segments in the delaminated region are also constrained from separating from each other, thus preventing any opening along the delamination surfaces that may occur. This is referred to as the *constrained-contact* model and introduces the constraint equation $w_k = w_{k+1}$ between the delamination surfaces of beam segments k and $k + 1$.

The second method is to assume no contact interaction between the beam segments in the delaminated region. This allows opening along the delamination surfaces; however, interpenetration can occur, $w_k \neq w_{k+1}$. This is referred to as the *unconstrained-contact* model.

The final method is to consider elastic contact along the delamination surfaces. The elastic contact is approximated using a Winkler foundation of linear springs, which represent the through-thickness stiffness of the contacting beam segments and act to resist interpenetration along the delamination surfaces. The stiffness of the springs for a contacting beam segment k is determined by considering one dimensional tension or compression of a beam element of height $h_k/2$. This model neglects shear deformations in the beam segment, which would lead to coupling of the springs (see Kerr (1964) for an in-depth discussion of foundation models), in accordance with what has been assumed initially. The stiffness of the layer of springs representing contact between two beam segments, k and $k + 1$, is given by:

$$k_{k,k+1}(x) = H(w_k(x) - w_{k+1}(x)) \frac{2E_T}{h_k + h_{k+1}}, \quad (5)$$

where E_T is the through-thickness modulus of the material ($E_T = E$ for an isotropic material) and $H(\cdot)$ is the Heaviside step function, $H(\xi) = \{1, \xi > 0; 0, \xi < 0\}$, which ensures that the springs resist only interpenetration and do not resist opening between beam segments. The pressure exerted at the bottom and top of beam segments k and $k + 1$ then follows as:

$$p_{k,k+1}(x) = k_{k,k+1}(x)(w_k(x) - w_{k+1}(x)). \quad (6)$$

This method is referred to as the *spring-contact* model. Since the regions of contact and opening are generally not known a priori, the problem in this case becomes nonlinear.

It will be shown in the following that the *constrained-* and *unconstrained-contact* models define upper and lower bound solutions of the *spring-contact* model. Both models can be recovered from the *spring-contact* model by taking the appropriate limit of the spring stiffness in Eq. (5). For the *constrained-contact* model, the limit $k_{k,k+1} \rightarrow \infty$ results in the constraint equation already defined, $w_k = w_{k+1}$. For the *unconstrained-contact* model, the limit as $k_{k,k+1} = 0$ results in $p_{k,k+1}(x) = 0$, namely the absence of any contact pressure. The *constrained-* and *unconstrained-contact* models, while less accurate than the *spring-contact* model, have the advantage of leading to closed form solutions of the problem in cases that require a numerical solution when treated with the *spring-contact* model. The solutions obtained with the simplified models are qualitatively similar to those of the *spring-contact* model and they can lead to insightful conclusions.

The proposed model relies on the three simplifying assumptions of zero shear deformation, absence of relative beam root rotations at the crack tips and non-frictional contact. The influence of shear deformation on the solution of single delamination problems is known to affect only quantitative details of the solution and to be negligible if the delamination is sufficiently long. In multiple delamination problems a stronger effect is expected when the delamination tips are close. However, current studies (Andrews et al., 2005) show that this effect is not strong in the absence of contact near the delamination tips and is negligible compared to the effect of unequal beam rotations at the delamination tips in the presence of contact.

The influence of the assumption of equal beam rotations at the crack tips has been shown previously to affect only quantitative details of the solution for single delaminations, leading to limited underestimation of the compliance of the system and the energy release rate for mode I fracture problems and to negligible effects in mode II fracture problems. In the presence of multiple delaminations the effect of the assumption is expected to be stronger due to the presence of contact between the crack faces. Different methods for correcting root rotations have been proposed since the early work of Kanninen (1973, 1974) (see for instance Williams, 1989; Sun and Pandey, 1994; Pandey and Sun, 1996; and Wang and Qiao, 2004). All methods, however, complicate the solution of the problem and as the crack interaction effects examined in this work will arise independently of the quantitative details of crack face phenomena, a simpler level of approximation has been utilized for this work.

Accounting for the presence of friction between the crack surfaces does not complicate the model greatly and could lead to interesting alterations of the results presented in this paper for certain geometries. This effect is not studied here and is the topic of current work (Andrews et al., 2005). The assumptions of the model and their implications will be discussed further in Section 5.

2.2. Model solution

An arbitrary section of the beam shown in Fig. 1a may be intersected by m of the n delaminations in the beam. Using the compatibility, equilibrium and constitutive equations defined above, the governing differential equations for the beam segments intersected by the section are

$$EI_k w_{k,xxxx} + p_{k,k+1} = p_{k-1,k}, \quad k = 1, \dots, m+1, \quad (7)$$

$$EA_k u_{k,xx} = 0, \quad k = 1, \dots, m+1, \quad (8)$$

where the p 's are contact pressures between the beams, except for $p_{0,1}$ and $p_{m+1,m+2}$ which are externally applied pressures on the external surfaces of the section. Eq. (8), referring to the axial displacements, are not coupled and general solutions can be derived for all k 's. Similarly, Eq. (7), referring to the transverse displacements, are not coupled and can be solved analytically within the approximation of *unconstrained-contact*. Full coupling derives from the constraint equations, $w_k = w_{k+1}$, of the *constrained-contact* model that again allows for a closed form general solution.

For the *spring-contact* model, on the other hand, the p 's are given by Eq. (6), which results in a system of $m + 1$ coupled differential equations, Eq. (7). Because the springs representing contact do not act in tension, contact may not occur between all of the beam segments intersected by this section. The presence of traction-free crack surfaces simplifies the system of coupled Eq. (7) so that a set of subsystems characterized by a lower number of coupled variables and equations can be defined. The limit cases are those of full coupling of the w_k for $k = 1, \dots, m + 1$, when contact exists between all segments, and no coupling when all crack surfaces are opened. The coupled differential equations are linear with constant coefficients and the characteristic algebraic equations for the sub-systems can always be found. The general closed form solution of a subsystem composed of one free segment and of 2 or 3 contacting beam segments is shown in Appendix A. A subsystem of more than three beam segments generally requires numerical solution. General solutions of the subsystems for each section of the beam in all possible states of opening and contact can then be determined and used in the iterative procedure to define the regions of contact and opening.

The solution for the whole structure is determined by applying the kinematic and static boundary and continuity conditions to define the constants of integration, C_i , of the general solutions of systems (7) and (8). If the *unconstrained-contact* or the *constrained-contact* model is used, the problem can then be solved in closed form. If the *unconstrained-contact* model predicts no interpenetration between the crack surfaces, the solution is exact. In addition, the regions of crack face interpenetration predicted through the *unconstrained-contact* model give a first approximation of the regions where contact is expected to occur within the *spring-contact* model.

If the *spring-contact* model is used, the regions where crack face contact and opening take place are unknown a priori and must be determined by an iterative solution process. The iterative process is initiated by assuming an initial state of contact along the delamination surfaces. The beam segments formed by the divisions at the crack tips are further subdivided at all coordinates where there is a change in contact state along a delamination surface. At these coordinates, additional continuity conditions are imposed between subdivisions j and k , which correspond to Eqs. (4) with the contributions from beam segment $k + 1$ removed. A system of algebraic equations, corresponding to the boundary and continuity conditions at all divisions of the beam and the general solutions of the governing Eqs. (7) and (8), is constructed based on this assumed state of contact and is solved numerically for the unknown constants of integration, C_i . Utilizing the displacement solution, updated regions of delamination surface interpenetration and opening are determined for all delaminations in the system. The updated regions of interpenetration are then assumed to be in contact and a new system of algebraic equations is constructed and solved for the new C_i 's. A grid of points is introduced along the axis of each beam segment and the convergence of the solution is checked by considering the norm of the transverse displacements at these locations. The process is repeated until convergence of the solution to a specified tolerance. For all cases examined in this paper, convergence of the solution has been reached easily with only a limited number of iterations.

2.3. Energy release rate and mode decomposition

It is assumed that the n delaminations in the structure are constrained to propagate along the low toughness fracture paths defined by their planes. The energy release rate for the individual coplanar extension of a delamination tip in this system is determined by application of the J -Integral (Rice, 1968) along a

path around the delamination tip. The expression for the J -integral for crack tip i , at the coordinate x_i , separating beam segments j , k and $k + 1$ (Fig. 1c), is

$$\mathcal{G}_i = J = \frac{1}{2} \left(\frac{M_k^2}{EI_k} + \frac{N_k^2}{EA_k} + \frac{M_{k+1}^2}{EI_{k+1}} + \frac{N_{k+1}^2}{EA_{k+1}} - \frac{M_j^2}{EI_j} - \frac{N_j^2}{EA_j} \right) \Big|_{x_i} \quad (9a)$$

This expression is identical to the expression valid for beams with a single delamination, as is explained in the following. Each crack tip in the beam shown in Fig. 1a can be extracted from the structure as an equivalent beam with a single delamination whose upper and lower surfaces are defined either by the surfaces of the plate or by other delaminations, Fig. 1c. This equivalent single beam is subject to end forces and moments as well as possible contact pressures on its upper and lower surfaces. The path for the J -integral, shown in Fig. 1c, is taken at the crack tip cross sections immediately preceding and following the crack tip and along the upper and lower surfaces of the equivalent beam. For this path, the contact pressures on the upper and lower surfaces do not enter the expression for the J -integral. If there is another delamination tip at the same coordinate x_i the energy release rate is determined as the limit for Δx_i tending to zero of Eq. (9a) applied to a system in which the length of the delamination of interest has been increased (the sign of Δx_i is chosen corresponding to an increase in delamination length) by incrementing the position of the crack tip to $x_i + \Delta x_i$. Expression (9a) is only valid when the rotations of the beams at the crack tips are assumed to be the same, and must be modified accordingly if this assumption is relaxed (see Section 5). Similarly, the equation could be modified to include the contributions due to the shear deformations along the beams.

The above approach cannot be applied to analyze the simultaneous propagation of m delamination tips that have the same coordinate x_m . Instead, the energy release rate in this case is conveniently determined by the variation of the total potential energy with respect to simultaneous unit extension da . The energy release rate for each of the delaminations under this condition is

$$\mathcal{G}_i = \frac{1}{m} \frac{dW}{da}, \quad (9b)$$

where W is the total potential energy of the system. The value of da should be chosen such that it corresponds to an increase in length of the delaminations. For the coordinate system described in Fig. 1, the extension of the left tips of delaminations corresponds to $da = -dx_m$ and the extension of the right tips of the delaminations corresponds to $da = dx_m$. The variation of the total potential energy is also used to analyze the simultaneous propagation of m delamination tips that do not share the same coordinate.

The conditions at the crack tips in the general beam of Fig. 1a are generally mixed mode. The energy release rate calculated using Eqs. (9a) and (9b) includes both the mode I and mode II components, \mathcal{G}_{Ii} and \mathcal{G}_{IIi} . Separation of the modes of fracture is accomplished by using the method proposed by Suo (1990), Suo and Hutchinson (1990) and Hutchinson and Suo (1992). They derived analytical expressions for the mixed mode stress intensity factors for a beam with a single crack, with total energy release rate given by Eq. (9a), in terms of the stress resultants, bending moments and normal forces, at the cross sections immediately preceding and following the crack tip, and geometrical parameters. These expressions depend on an additional parameter that can be derived with a rigorous two-dimensional solution of the problem. In the model proposed in this paper, the method is applied to the equivalent beam with a single crack shown in Fig. 1c with energy release rate given by Eq. (9a) and is thus valid for each crack tip in the system.

3. Cantilever beam with n equal length delaminations

The first study problem is a cantilever beam of length L with n through width, arbitrarily spaced edge delaminations (Fig. 2) subjected to a static concentrated out of plane force P at its free end. This simple

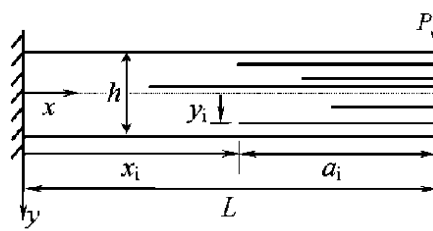


Fig. 2. Cantilever beam with n edge cracks subject to a transverse load P .

structure provides an analytical/semi-analytical description of how multiple delaminations interact. This problem yields results that are identical to those for an edge cracked simply supported beam, loaded by an out of plane force at its mid span. Solutions for simply supported or fixed plates with mid-span, out of plane loading can be simply obtained by modifying the boundary conditions at $x = 0$ and $x = L$. The solution can also be easily extended to circular axisymmetric plates loaded by concentrated out of plane forces at the centers.

In this problem no axial forces are developed; thus the equations governing the axial displacements are ignored. The boundary conditions for this problem are

$$\begin{aligned} w_0 &= 0, & w_{0,x} &= 0 & \text{at } x &= 0, \\ P &= \sum_{k=j}^{j+n} V_k, & M_k &= 0, & k &= j, \dots, j+n, \\ w_k &= w_{k+1}, & k &= j, \dots, j+n-1 & \text{at } x &= L, \end{aligned} \quad (10)$$

where j is the index of the uppermost beam segment at the free end of the beam; and as before, the subscripts define the number of the beam segments. Contact of the beam segments under the load point is approximated by assuming that their deflections at the free end are equal. This assumption is exact for the *unconstrained-contact* model and accurate for the *spring-contact* model if the delaminations are long. The static and kinematic continuity conditions at each crack tip are given by Eq. (4).

In the simplest configuration, the delaminations in the beam shown in Fig. 2 are of the same length a . In this configuration, the beam is divided up into $n + 2$ beam segments, $n + 1$ segments forming the cracked region, and one segment forming the uncracked region. Each crack tip is located at the same coordinate $x = L - a$. The continuity conditions (4) are modified as follows:

$$\begin{aligned} w_0 &= w_k, & w_{0,x} &= w_{k,x}, & k &= 1, \dots, n+1, \\ M_0 &= \sum_{k=1}^{n+1} M_k, & V_0 &= \sum_{k=1}^{n+1} V_k. \end{aligned} \quad (11)$$

Combining the general solutions for each beam segment for the three contact models allows this system of $4(n + 2)$ boundary and continuity equations to be solved in closed form (Appendix B). The three methods yield identical solutions, which shows that the deflections of the beam segments in the cracked region of the beam are identical and there is no contact or opening along the crack faces.

3.1. Energy release rates for simultaneous propagation of equal length delaminations

The energy release rate for each delamination when the delaminations are assumed to propagate simultaneously is conveniently determined by the variation of the total potential energy W due to a unit propagation of the cracks, Eq. (9b):

$$\mathcal{G}_i = \frac{1}{n} \frac{dW}{da} = \frac{1}{2n} \frac{P^2 a^2}{EI_0} \left(I_0 / \sum_{k=1}^{n+1} I_k - 1 \right), \quad (12)$$

where I_0 is the moment of inertia of the intact portion of the beam and I_k is the moment of inertia of the beam segment in the cracked portion of the beam. The next sections will show that for n equally spaced delaminations the energy release rate for simultaneous propagation is higher than the energy release rate corresponding to the propagation of one of the delaminations of the system. On the other hand, when the delaminations are unequally spaced, the response is controlled by the transverse position of the delaminations.

Eq. (12) shows that if the delaminations are uniformly spaced across the entire cross section, then as the number of delaminations increases, the energy release rate per delamination also increases. If on the other hand, the cracks are confined to a band, then as the number of cracks within the band increases the energy release rate per crack decreases. The latter case could represent damage localization in the beam. If a crack growth criterion based on the total energy release rate is applied, the first case would correspond to a decrease of the critical load on increasing the number of cracks, and the second case to an increase of the critical load. However, for the second case, since the cracks are not equally spaced, the assumption of simultaneous propagation may not be valid and the critical load could be defined by the propagation of only one of the cracks of the system.

3.2. Stability of the equality of length in a system of equal length delaminations

The equality of length will be said to be stable in a system of equal length delaminations if the system recovers the condition of equal length after the lengths of one or more cracks are perturbed.¹ It will be shown later that, for a fixed number of delaminations, the energy absorption is higher if the equality of length is stable than if it is not.

3.2.1. Equally spaced delaminations

This special case was previously examined by Suemasu and Majima (1996) who investigated the stability of the equality of length of an axisymmetric system of equally spaced, penny-shaped delaminations in a clamped circular plate subject to a concentrated out-of-plane load. The study was performed under the simplifying kinematic assumption of *constrained-contact*. This assumption is relaxed here, and the stability of the equality of length is studied using the *spring-contact* model. The problem is greatly simplified by noting that in the limit of the delaminations having the same length, the solution of the *spring-contact* model is identical to that of the *unconstrained-contact* model. Closed form solutions can therefore be found, which are detailed in Appendix C and summarized below.

An ideal system of equal length, equally spaced delaminations propagates when the energy release rate, given by Eq. (12), equals the fracture energy of the material. If a positive perturbation of the length of crack i in the system is considered, then the energy release rate for the propagation of that crack is lower than that corresponding to the simultaneous propagation of the remaining cracks. Thus, using a fracture criterion based on the total energy release rate, the remaining delaminations will grow up to the length of the perturbed delamination and equality of length will be restored. Conversely, if a negative perturbation of the length of crack i is considered, then the energy release rate of crack i is higher than that of the remaining cracks: the system is again stable. Since a negative perturbation of one crack is identical to a positive perturbation

¹ The term stability is used here to refer to changes in the crack geometry and *not* the question of whether the crack growth is quasi-static (stable) or dynamic (unstable).

of the remaining cracks and vice versa, conclusions on the effect of positive or negative perturbations of one crack will also hold for perturbations of a generic number of cracks.

The same conclusions are reached if the simplifying kinematic assumption of *constrained contact* is used. The analysis, which is similar to that presented in the [Appendix C](#), is not presented here. Suemasu and Majima (1996) obtained the same results for axisymmetric clamped circular plates.

3.2.2. Unequally spaced delaminations

A system of unequally spaced, equal length delaminations does not always grow self-similarly, even in the absence of length perturbations. The question of stability of the equality of length is controlled by the through-thickness position of the delaminations. The map of [Fig. 3](#) refers to a two-crack system and has been constructed by using the *spring-contact* model. Similar results are obtained using the *unconstrained-contact* model. [Fig. 3](#) shows regions in which the energy release rates for the propagation of one of the two cracks, \mathcal{G}_U and \mathcal{G}_L , and for their simultaneous propagation, \mathcal{G}_B , have different ordering. The map is a function of the through-thickness positions of the two cracks. The upper crack is located at a distance h_3 from the upper surface of the beam and the lower crack is located at a distance h_5 from the lower surface of the beam, as shown in the inset in the figure.

The map shows three regions: region I in which $\mathcal{G}_U > \max(\mathcal{G}_L, \mathcal{G}_B)$; region II in which $\mathcal{G}_B > \max(\mathcal{G}_U, \mathcal{G}_L)$; and region III in which $\mathcal{G}_L > \max(\mathcal{G}_U, \mathcal{G}_B)$. Thus in regions I and III, only one crack will propagate when critical conditions are satisfied, while in region II, both cracks propagate together. Furthermore, in regions I and III, the system is more unstable (increasing difference between the highest and next highest values of \mathcal{G}_U , \mathcal{G}_L , and \mathcal{G}_B) under positive perturbations of the length of the upper crack (region I) and to negative perturbations of the length of the lower crack (region III).

For cases lying in region II the system is stable to both positive and negative perturbations. Thus, in this region the delaminations will always grow self-similarly. The solution of equally spaced delaminations is represented in the diagram by a point in the shaded pocket at $h_3 = h_5 = 1/3h$.

In the case of unequally spaced delaminations, the *constrained-contact* model yields a map with a larger region of stability than that shown in [Fig. 3](#). The region is shown in [Fig. D.1b](#). This difference highlights the limitations of the simplified contact models when applied to general delamination geometries.

In a real structure, the location of the delaminations through the thickness of the plate will depend on the internal structure of the material and the loading conditions, which therefore determine the conditions for the stability of the equality of length of the system.

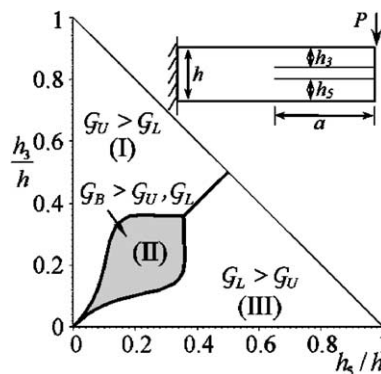


Fig. 3. Map of regions of different energy release rate for a system with two cracks.

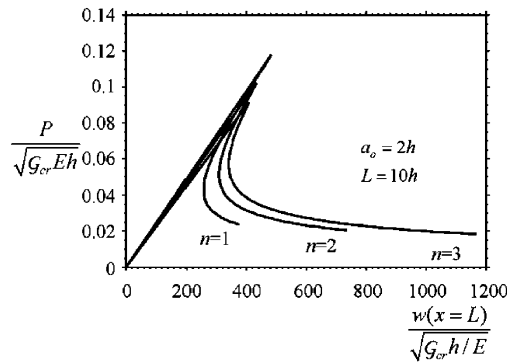


Fig. 4. Dimensionless diagram of the critical load for crack propagation versus load–point displacement for a cantilever beam of n equal length and equally spaced cracks.

3.3. Macrostructural response

The macrostructural behavior of a plate of length $10h$ with n equally spaced delaminations, $h_k = h/(n+1)$, of equal initial length $a_0 = 2h$ is shown in Fig. 4. The delaminations have been assumed to propagate when $\mathcal{G}_i = \mathcal{G}_{cr}$, where \mathcal{G}_{cr} is the fracture energy of the material. The figure shows the normalized critical load for the propagation of the crack system as a function of the normalized load point displacement. As the number of delaminations increases, the critical load for initial growth of the delaminations decreases and the post-peak behavior of the structure becomes more ductile. This is to be expected as diffuse damage leads to a more ductile structural response and increased energy absorption. In contrast, localized damage, for instance the propagation of a single crack, results in an increased ultimate capacity of the structure, but in a less ductile response and decreased energy absorption.

4. Cantilever beam with two unequal length delaminations

In a general system of delaminations with unequal length and spacing, Eq. (12) and the conclusions and results of the previous section do not apply and the general problem defined by Eq. (7) must be solved in order to define energy release rates. In this section, a system of only two cracks is studied, in which many of the characteristics expected of general cases can be observed, without distracting complexity. In most cases, the behavior of the system depends on only three dependent variables, allowing complete visualization of the interaction effects.

A cantilever beam of length L and height h with two edge delaminations of arbitrary length and spacing is shown in Fig. 5. The length of the upper delamination is a_U and the length of the lower delamination is a_L . The through-thickness positions of the delaminations are defined by h_3 and h_5 , where h_3 is the distance of the upper delaminations from the upper surface of the beam and h_5 is the distance of the lower delamination from the lower surface of the beam. Utilizing the three approximations for treating contact, the system of equations formed by the boundary conditions Eqs. (10) and continuity conditions Eqs. (4) together with Eq. (7) has been solved for the three possible configurations of the system, $a_U = a_L$ (Section 3), $a_U > a_L$ (Fig. 5a) and $a_U < a_L$ (Fig. 5b).

4.1. Energy release rate

Solutions for the energy release rate of the different configurations of the system are presented in Appendix D. Appendix A also presents in Fig. D.1 maps constructed for a general through-thickness distribution

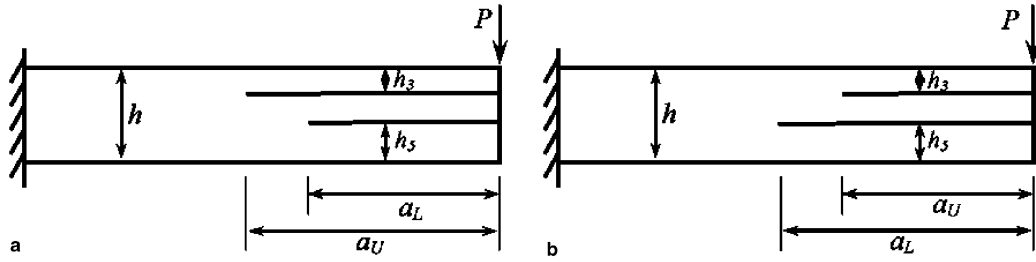


Fig. 5. Cantilever beam with two arbitrarily spaced cracks.

and lengths of the delaminations that show regions in which the energy release rate of one of the cracks is higher or lower than that of the other crack and can be used to analyze crack propagation in the system.

Fig. 6 shows exemplary solutions for a system of two equally spaced cracks ($h_3 = h_5 = h/3$). Fig. 6a defines the energy release rate of the upper crack on varying its length, while the length of the lower crack is kept fixed at $a_L/h = 5.0$. Fig. 6b defines the energy release rate of the lower crack on varying its length, while the length of the upper crack is kept fixed at $a_U/h = 5.0$. The figures show a comparison of the energy release rates calculated using the three approximations of contact (solid curve = *spring-contact*, dashed curve = *unconstrained-contact* and dash-dot curve = *constrained-contact*). Numerical results from these figures and others show that the *unconstrained-contact* and *constrained-contact* models define upper and lower bounds of the *spring-contact* model for all through-thickness distributions of the cracks. Fig. 6 also shows by the

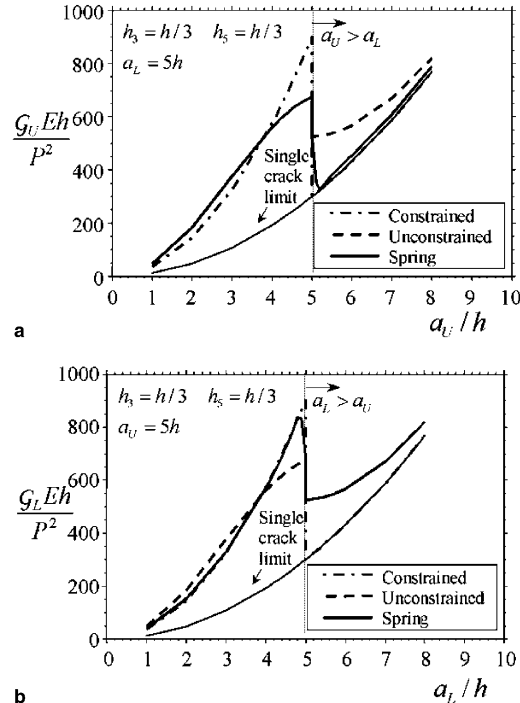


Fig. 6. Normalized energy release rates of two equally spaced cracks in the beam of Fig. 5 as a function of the length of the cracks. (a) Upper crack, (b) lower crack.

thin line the energy release rate of the crack in the absence of the other crack, or the single crack limit. The limit is approached when the interaction effects disappear. The *constrained-contact* model reaches this limit immediately after the discontinuity in energy release rate. Zheng and Sun (1998) showed similar behavior for the longer delamination of two central, through-width delaminations in a three-point bending specimen.

Fig. 6a and b show that in the equally spaced delamination system studied there is a strong interaction effect on the energy release rate, which is always amplified with respect to the single crack solution. The next section will show that different solutions, characterized by shielding, amplification or a combination of both, are found for other crack systems. In addition seems out of place reach the same length there are negative discontinuities of the same magnitude in their energy release rates. It will be shown in Section 5 that the discontinuity is a good approximation of a sharp change in energy release rate shown by a full numerical solution of the problem. In other material systems a similar behavior has been observed. For instance, from the 2-D solution of an infinite body with a main crack interacting with ordered arrays of micro-cracks, sharp jumps in the stress intensity factors have been noted as the main crack tip moves through the array (Brenich and Carpinteri, 1996).

4.2. Shielding and amplification of the energy release rate

As observed in the previous section, a delamination in a system of delaminations can either amplify or shield the energy release rates of the other delaminations or have no influence on them. This effect can be synthesized for the crack system of Fig. 5 by considering diagrams of the energy release rate of a crack, \mathcal{G}_i , normalized with respect to the energy release rate of the same crack when the other crack is not present, \mathcal{G}_{i0} .

The energy release rate of a crack is always amplified by the presence of a shorter crack independent of their through-thickness positions, which only affect the magnitude of the amplification (the *constrained-contact* model erroneously predicts for this regime neither amplification or shielding). A longer crack can have different effects on a shorter crack, with the sense of the effect depending on their through-thickness positions and, in some regimes, their lengths. The maps shown in Fig. 7a and b have been obtained using the *spring-contact* model (identical results are obtained assuming *unconstrained-contact*). The dashed lines in the figures are solutions of the *constrained-contact* model.

If the point describing the positions of the two delaminations falls in the upper region (III), the shorter delamination will always be shielded by the longer. The magnitude of the shielding effect depends on their

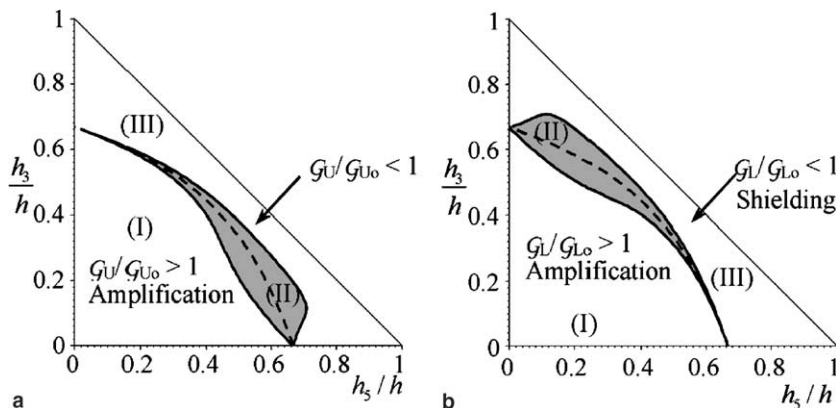


Fig. 7. Map of shielding and amplification of the energy release rate for a crack in the presence of a longer crack (schematic of Fig. 5). Shaded regions (II) indicate a combination of shielding and amplification depending on the length of the delaminations. (a) Upper crack, (b) lower crack.

lengths. If the point falls in the lower region (I), the energy release rate of the shorter delamination will always be amplified by the longer. If the point falls in the middle region (II), either amplification or shielding can occur for the shorter crack, depending on the two lengths. The solution of the *constrained-contact* model does not have a region of mixed shielding and amplification. The dashed line in Fig. 7 corresponds to crack configurations where $\mathcal{G}_L = \mathcal{G}_{L0}$ and separates regions of shielding (III) and amplification (I). This simplified model is unable to predict the complex details of multiply delaminated systems.

An example considering the energy release rate of the lower delamination for a through-thickness position of the cracks that falls in region (I), showing amplification of \mathcal{G}_L , is presented in Fig. 8a. The figure shows \mathcal{G}_L normalized with respect to \mathcal{G}_{L0} on varying a_L with the length of the upper crack fixed at $a_U/h = 5.0$. When the lower crack is shorter than the upper crack, there is a strong amplification of \mathcal{G}_L with

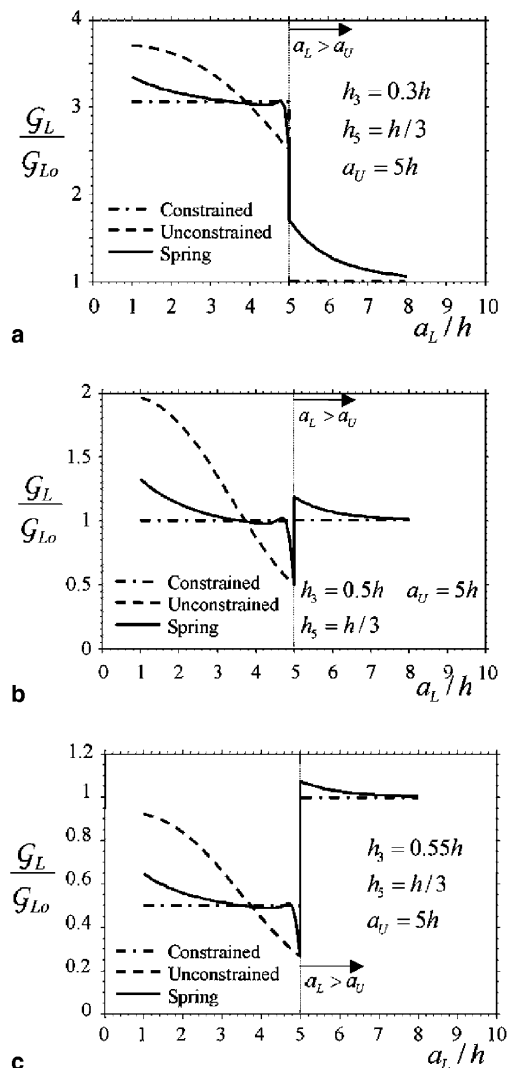


Fig. 8. Examples of shielding and amplification of the energy release rate of the lower crack in the two-crack system of Fig. 5 (upper crack length fixed).

an amplification factor around 3. The amplification is then reduced by the discontinuity (localized shielding effect), when the two cracks have the same length, and it decreases on increasing the length of the crack. An example of shielding of \mathcal{G}_L , a point in region (III), is shown in Fig. 8c. In this case the discontinuity in \mathcal{G} corresponds to a localized amplification effect. An example of both shielding and amplification depending on the lengths of the delaminations, a point in region (II), is shown in Fig. 8b.

In this structure the shielding of one of the delaminations is always accompanied by the amplification of the other delamination. Among all the possible through-thickness distributions and lengths of the delaminations, the effect of the interaction can be very strong, and it has been verified numerically that the energy release rate can be amplified up to 600% by the presence of a much longer delamination.

Brencich and Carpinteri (1996) showed qualitatively similar amplification and shielding effects when considering the interactions of a main crack propagating through a pair of symmetrically located micro-cracks in an infinite body. For this problem the magnitude of the shielding and amplification depends on the spacing between the cracks, but the qualitative behavior of the shielding and amplification is unaffected by this distance. In contrast, for the structural delaminations discussed in this paper, due to geometrical effects, the through-thickness position of the delamination may alter the condition of shielding or amplification, not just their magnitudes. This is in agreement with the numerical study of the interaction of two central delaminations in a three-point bending specimen of Zheng and Sun (1998).

4.3. Mode ratio

Mode decomposition has been performed for the exemplary system of two equally spaced delaminations. Fig. 9 shows the relative amount of mode II to mode I defined by the phase angle $\Psi = \tan^{-1}(K_{II}/K_I)$. Fig. 9a defines Ψ_U for the upper delamination on varying its length, while the length of the lower delamination

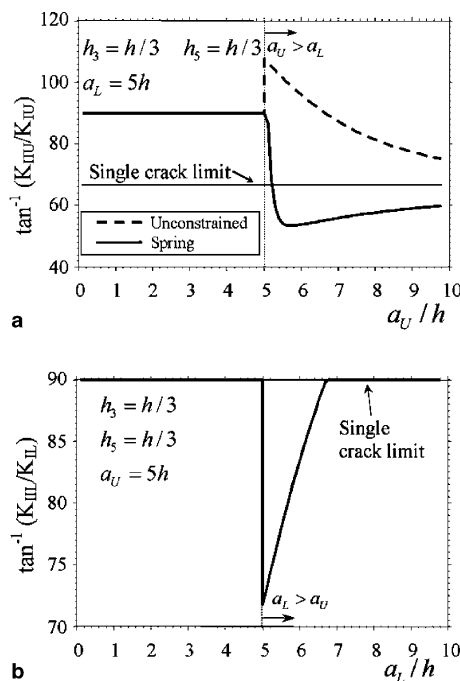


Fig. 9. Relative amount of mode II to mode I stress intensity factors in the two-crack system of Fig. 5.

is kept fixed at $a_L/h = 5.0$. Fig. 9b defines Ψ_L for the lower delamination on varying its length, while the length of the upper delamination is kept fixed at $a_U/h = 5.0$.

The figures compare solutions obtained using the *spring-contact* model (thick solid line) with the *unconstrained-contact* model (dashed line) and the solution of a single delamination Ψ_0 , in the absence of the other delamination (thin line). For a single delamination, the relative amount of mode II to mode I is independent of the delamination length and given by $\Psi_{U0} = 66.7^\circ$ for the upper delamination and by $\Psi_{L0} = 90^\circ$ for the lower delamination (the lower delamination experiences pure mode II conditions due to localized contact at the crack tip).

Fig. 9a shows that when the upper delamination is shorter than the lower, the conditions are pure mode II. Comparison with the single delamination solution highlights the strong effect produced by the presence of the lower delamination. When the upper delamination reaches the length of the lower delamination there is a sharp transition and the mode I component is suddenly increased above the corresponding single delamination solution (thin line). As the upper crack lengthens, the interaction decreases and the solution tends to the single delamination limit. The dashed curve highlights the limitations of the simplified *unconstrained-contact* model, which predicts an unrealistic phase angle $\Psi > 90^\circ$, due to the interpenetration of the delamination surfaces.

Fig. 9b shows that the lower delamination is in pure mode II conditions due to contact at the delamination tip when its length is shorter than the length of the upper delamination and this solution coincides with the solution of the single delamination. When the lower delamination approaches the length of the upper delamination, there is a sudden transition (solid curve) to a large value of the mode I component. The interaction effect then disappears quickly as the lower delamination lengthens and the solution tends again to the solution of a single delamination. Interestingly, when the lower delamination is longer, the bending theory model always predicts opening at the lower delamination tip even when the mode decomposition method defines a negative mode I stress intensity factor and therefore pure mode II conditions (shown in Fig. 9b for $a_L/h > 6.75$). This fictitious opening displacement field is a consequence of neglecting the root rotations at the delamination tip, which if properly accounted for would restore contact (Andrews et al., 2005).

4.4. Delamination growth and macro-structural behavior

To investigate the macro-structural response of the plate, the quasi-static propagation of the system of two delaminations shown in Fig. 5 has been studied using the *spring-contact* model. A delamination has been assumed to propagate when its energy release rate equals the fracture energy of the material, \mathcal{G}_{cr} . The cracks have been assumed to grow under delamination length control, which allows virtual delamination growth branches to be followed. Several cases, identified by different through-thickness positions of the delaminations and different notch lengths as shown in Figs. 10–13, have been considered to highlight a number of interesting macrostructural responses of the system. The figures show the critical load for crack propagation as a function of the load point deflection. Also shown in the inset in the figures is the evolution of the lengths of the delaminations; the dashed line shows the length of the lower delamination and the solid line shows the length of the upper delamination during the loading process.

For the first delamination configuration, shown in Fig. 10, the lower delamination starts to propagate first at (A). The propagation is unstable up to point (B), where the delamination reaches the upper delamination. At this point the delamination arrests and the delamination system can be made to propagate only by increasing the applied load. This behavior is due to a negative discontinuity, shielding, in the energy release rate. After point (C) the lower delamination continues to propagate unstably until the structure fails. A snap-back instability is present as the lower delamination grows to the upper delamination.

In the case shown in Fig. 11 the lower delamination begins to propagate unstably at point (A). At (B) the delaminations are of the same length and there is a sudden drop in the critical load, corresponding to a

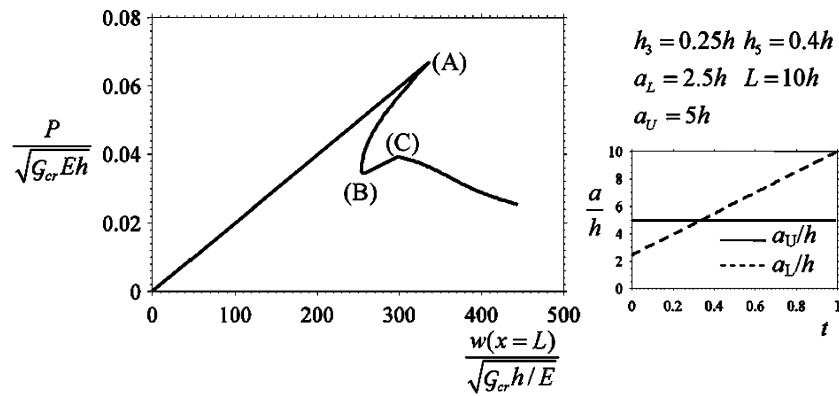


Fig. 10. Dimensionless diagram of the critical load for crack propagation versus load–point displacement in the two-crack system of Fig. 5: snap-back instability and local increase in critical load due to a local shielding effect.

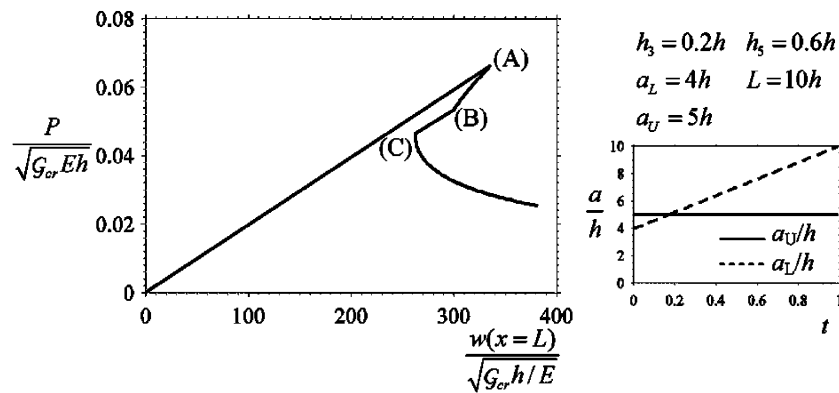


Fig. 11. Dimensionless diagram of the critical load for crack propagation versus load–point displacement in the two-crack system of Fig. 5: snap-back instability with local drop in critical load due to a local amplification effect.

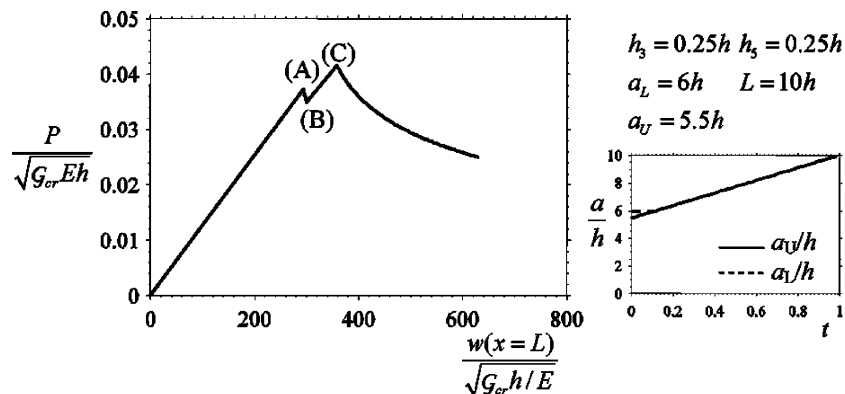


Fig. 12. Dimensionless diagram of the critical load for crack propagation versus load–point displacement in the two-crack system of Fig. 5: snap-through instability and hyper-strength phenomenon due to a local shielding effect.

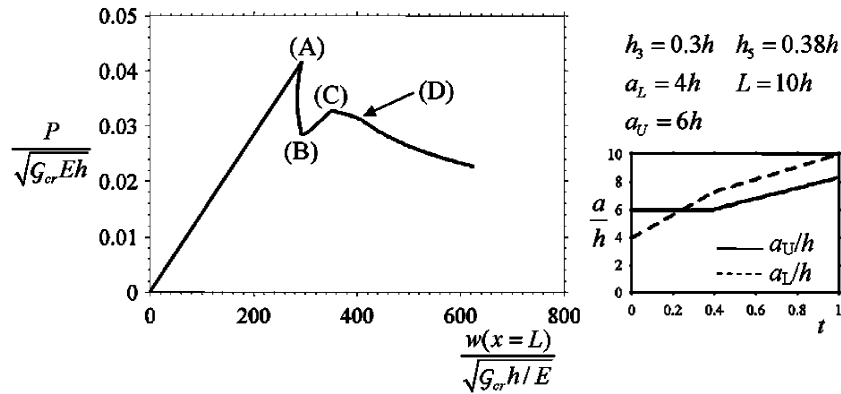


Fig. 13. Dimensionless diagram of the critical load for crack propagation versus load–point displacement in the two-crack system of Fig. 5: crack pull along.

positive discontinuity, amplification, of the energy release rate. The lower delamination then continues to propagate unstably.

The case shown in Fig. 12 is similar to that examined in Fig. 10. However in this case the new critical load due to the negative discontinuity, shielding, in the energy release rate is higher than the initial load for delamination propagation. This is an interesting example of hyperstrength, which is defined as the condition that the ultimate load of the structure exceeds the load corresponding to the first propagation of one of the delaminations of the system even in the absence of any strengthening mechanisms. The hyperstrength is produced by the elastic interactions of the parallel delaminations that create local shielding and hardening effects, leading to a snap-through instability.

An example of crack pull-along, in which the finite propagation of one delamination causes the propagation of the other delamination, is shown in Fig. 13. In this case the lower delamination propagates first at point (A). When it reaches the second delamination at point (B), there is an increase in critical load due to a negative discontinuity in energy release rate. The lower delamination continues to propagate at point (C). At point (D), the upper delamination begins to propagate, and both delaminations continue to propagate, keeping a constant relative length until the structure fails. This behavior occurs for through-thickness distributions of the delaminations that fall just to the right or just above the shaded region of the map of Fig. D.1a, and just to the right of the shaded region in the map of Fig. D.1b.

5. Validation of the proposed model

The proposed model, applied to the problem of a cantilever beam with two edge cracks, has been validated using the finite element method (FEM) and the commercial code ANSYS (5.5). The mesh consisted of plane stress isoparametric triangular elements. To obtain an accurate solution, including relative crack displacements, while keeping the number of degrees of freedom low, a coarse mesh was used for the body of the beam and very fine meshes around each crack tip and along areas of contact. The stress singularities at the crack tips were modeled with rosettes of quarter point elements. Contact along the crack faces was simulated using gap elements that prevent interpenetration of the beams with stiff linear springs. Convergence of the solution was checked by varying the size and number of elements and stiffnesses of the gap springs. Energy release rates were calculated by two methods, the J -Integral, Rice (1968), and the displacement correlation method, Chan et al. (1970), which was also used to evaluate the mode ratio. The path of the J -integral was chosen within a fine mesh region so that it encompassed sufficient elements for its value to converge.

5.1. Comparison of energy release rates

The energy release rates determined by the finite element method and the present *spring-contact* model are shown in Fig. 14a for a system of two equally spaced cracks ($h_3 = h_5 = h/3$). The error between the two solutions is shown in Fig. 14b. In the figure, the normalized energy release rate of the upper crack is depicted as a function of the length of the upper crack. The length of the lower crack is kept fixed at $a_L/h = 5.0$.

Fig. 14a and b show that the results of the proposed model generally agree with the finite element results. When the cracks reach the same length, the finite element solution predicts a continuous transition in energy release rate. This transition matches the discontinuity in energy release rate predicted by the beam theory model.

Short cracks ($a_U < 2h$ for the geometry of Fig. 14) are characterized by large errors due to the well-known limitations of classical beam theory. As expected, the error drops when the length of the crack increases, provided it is not similar to the length of the other crack, to less than 5% when $2h < a_U < 4.6h$ or $a_U > 7.0h$. Where the two cracks have similar lengths and the energy release rate is characterized by a discontinuity, the error increases significantly (up to 30% for the geometry studied in Fig. 14). The width of this region is given by a few times the separation of the planes of the interacting cracks and depends on the conditions of the crack surfaces (contact or opening). For the geometry studied in Fig. 14, the error is above 5% for $4.6h < a_U < 7.0h$. The interval is not symmetric about the length of the lower crack, $a_L = 5h$, because of the different conditions along the crack surfaces when the upper crack is shorter (opening) or longer (contact) than the lower. Numerical calculations show that behaviors similar to that observed in Fig. 14 characterize all possible crack configurations and that the width of the region where the error increases significantly is always a few times the distance between the planes of the cracks.

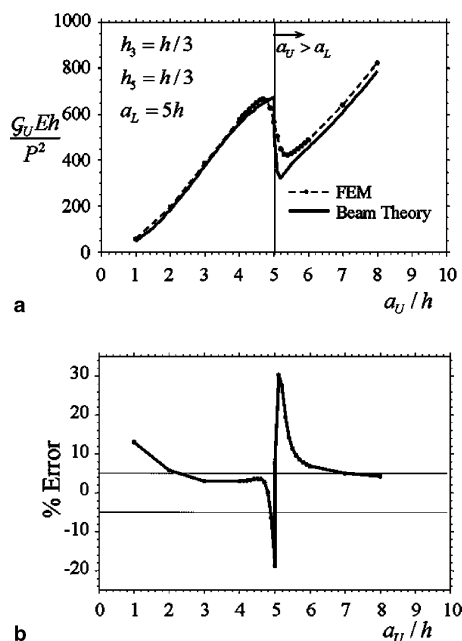


Fig. 14. (a) Energy release rate of the upper crack in the two-crack system of Fig. 5: comparison between FE and proposed model results. (b) Relative error between the solutions of (a) (dashed line indicates a 5% relative error).

5.2. Comparison of mode ratios

The relative amount of mode II to mode I as measured by the phase angle $\Psi = \tan^{-1}(K_{II}/K_I)$ determined by the finite element method and the model presented in this paper utilizing the *spring-contact* approximation is shown in Fig. 15. Fig. 15a shows the phase angle of the upper crack as a function of the length of the upper crack, while keeping the length of the lower crack fixed at $a_L/h = 5.0$. Fig. 15b shows the phase angle of the lower crack while keeping the length of the upper crack fixed at $a_U/h = 5.0$.

The phase angles of the lower crack determined by the two models, shown in Fig. 15b, agree well with the relative error peaking near the discontinuity at only 10%. Fig. 15a instead shows a significant difference, with an error up to 26%, between the results of the bending theory model and FEM when the upper crack is longer and there is contact along both delamination surfaces. When the lower crack is longer and there is no contact along the delamination surfaces, the error is instead very low. This result confirms what has already been observed for the energy release rate. However, the width of the region where the relative error on the mode ratio is quite large and is greater than that corresponding to the energy release rate.

5.3. Discussion

The relative error between the model and the FE predictions, as observed in Figs. 14 and 15, is greater when there is contact between the crack surfaces. This is mainly due to the assumption of the proposed model of zero relative root rotations of the sublaminates at the crack tips that leads to an overestimation of the contact pressures. The effects of the root rotations on the contact pressures and thus on the energy release rate and mode ratio are most significant when the cracks are close to the same length $|a_U - a_L| < h$ and are stronger on the mode ratio. When there is no contact along the crack faces, neglecting the root

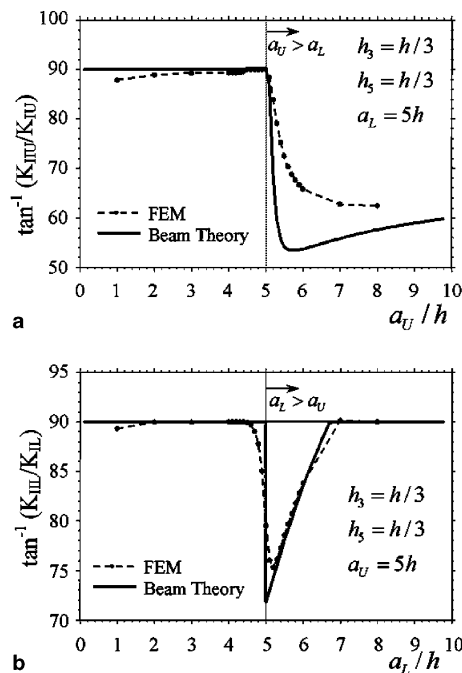


Fig. 15. Relative amount of mode II to mode I for a two-crack system: comparison between proposed model and FE results.

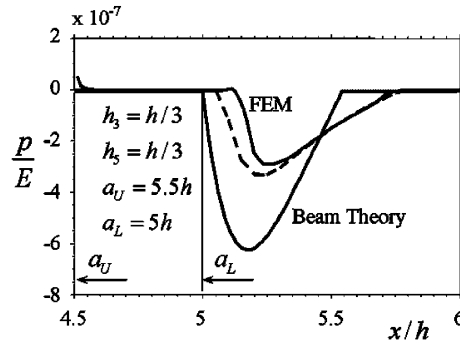


Fig. 16. Comparison of predicted contact pressures along the faces of the upper crack in the two-crack system (dashed line: contact pressures using the FE displacement field and *spring-contact* approximation).

rotations does not significantly affect the solution, confirming what has already been observed for single delaminations loaded primarily in shear.

The contact pressure distribution along the surfaces of the upper crack, for equally spaced cracks with lengths $a_U/h = 5.5$ and $a_L/h = 5$, predicted by the proposed model and the FE method are shown in Fig. 16 as a function of the position along the crack. The model predicts a peak pressure double that of the FE solution. These discrepancies in the solutions cannot be attributed to the contact approximation used in the model: using the centerline beam deflections obtained in the FE solution and Eq. (6) to predict the contact pressure leads to the pressures identified by the dashed curve that for magnitude and shape closely follow the finite element solution. Including shear deformations in the model improves the pressure distribution, but does not substantially improve the values of the energy release rate.

The overestimation of the contact pressures is associated with significant errors in the stress resultants at the crack tip. This is shown in Table 1 where bending moment and shear force obtained using the proposed model are compared with the FE results (rows 2 and 1). Table 1 also compares the energy release rates and phase angles obtained using the proposed model (row 2) and the FEM (row 1) and highlights the previously noted large errors. If the actual FE stress resultants are used instead of the model resultants in Eq. (9a) and in the expressions of Suo and Hutchinson for the stress intensity factors, the solution is still affected by large errors. This is shown in row 3 of the table. The reason for this discrepancy is that both Eq. (9a) for the energy release rate and Suo and Hutchinson's expressions do not account for the contributions due to the shear deformations along the beams and the deformations at the crack tip cross sections (i.e., root rotations).

The expression (9a) for the energy release rate can be modified to account for these effects as follows:

$$\mathcal{G}_i = J = \frac{1}{2} \left(\sum_{l=k}^{k+1} \left(\frac{M_l^2}{EI_l} + \frac{V_l^2}{\kappa GA_l} + \frac{N_l^2}{EA_l} - 2V_l\phi_l \right) - \frac{M_j^2}{EI_j} - \frac{V_j^2}{\kappa GA_j} - \frac{N_j^2}{EA_j} + 2V_j\phi_j \right) \Big|_{x_i}, \quad (13)$$

where \mathcal{G} is the shear modulus, κ is the shear correction coefficient (5/6 for a rectangular cross section), V and ϕ are the shear resultant and the bending rotation respectively.

Li et al. (2004) recently modified the stress intensity factor expressions derived by Suo and Hutchinson to include the contributions of the shear deformations along the beam and the crack tip deformations numerically. Wang and Qiao (2004) proposed an analytical extension of the method of Suo and Hutchinson. Rows (4) and (5) in the Table show solutions obtained using these two methods. Both methods lead to substantial improvement in the solutions. The method of Wang and Qiao relies on the assumptions of plate theory in order to determine the crack tip rotations, and thus is not as accurate as the numerical solution of Li et al.

Table 1
Stress resultants, energy release rate and phase angle of the upper crack

		Moment— upper beam arm (M/Ph)	Moment— lower beam arm (M/Ph)	Shear— upper beam arm (V/P)	Shear— lower beam arm (V/P)	Ψ_U , % Error from FEM	$\mathcal{G}_U Eh/P^2$, % Error from FEM
(1)	FE stress resultants \mathcal{G} and Ψ Displacement correlation Technique	−0.967	−4.535	−0.644	1.644	72.4°	428.59
(2)	Proposed model	−0.300	−5.200	−1.752	2.752	54.2°, 25.18%	380.89, 11.13%
(3)	FE stress resultants \mathcal{G} Eq. (9a) Ψ after Suo and Hutchinson	−0.967	−4.535	−0.644	1.644	80.9°, −11.66%	386.14, 9.91%
(4)	FE stress resultants \mathcal{G} , Ψ after Li and Thouless	−0.967	−4.535	−0.644	1.644	72.2°, 0.31%	430.18, −0.37%
(5)	FE stress resultants \mathcal{G} Eq. (13) Ψ after Wang and Qiao	−0.967	−4.535	−0.644	1.644	74.4°, −2.71%	417.65, 2.55%

Equally spaced cracks, $a_U/h = 5.5$, $a_L/h = 5$, $h/L = 0.1$.

The observations above highlight that the model proposed in this paper could be improved substantially by: removing the assumption of zero relative root rotations at the crack tips, for instance by using localized linear elastic rotational springs (Pandey and Sun, 1996); including the contribution of shear deformations along the beams; applying Eq. (13) for the energy release rate and an extended solution, e.g. of Li et al. (2004) or Wang and Qiao (2004), for the decomposition of the modes of fracture. This would lead to a more accurate quantitative prediction of the displacement fields along the crack surfaces and the fracture parameters of the system. Such an approach would become necessary, and would probably be sufficient for plane conditions, if the influence of crack-wake mechanisms, such as bridging or cohesive mechanisms and friction, on the fracture behavior of multiply delaminated plates is to be investigated.

6. Application of the proposed model to the design

6.1. Beam theory for quantitative analyses

Elastic analyses of laminates that are based on plate elements are widely used and accurate for many design predictions. Extended laminar sheets comprising thin plies do indeed very nearly satisfy the conditions of strain distribution necessary for the reduced degrees of freedom in beam (or plate) theory to be sufficient.

As shown in this paper, modeling delamination fracture is, however, much more challenging. In multiply delaminated beams as well as other more complex structures, delaminations propagate in mixed mode, often predominantly in shear (modes II and III). Crack propagation, even in the absence of a through-thickness reinforcement (stitching, pins, etc.), will therefore be very strongly and commonly influenced by contact forces and crack face friction. Other crack wake effects, such as bridging by fibers or craze fibrils, might also be important. The tractions imposed on the fracture surfaces by such effects will depend, possibly sensitively, on the mixed mode crack displacement vector; and therefore accurate prediction of the crack displacement becomes a prerequisite to a full quantitative model of delamination.

The question of whether plate or beam theory methods can deal with quantitative delamination analysis turns on the success of estimates of root rotations, which control the accuracy of crack displacement predictions near crack tips. Our current work and work in the literature (Andrews et al., 2005; Sun and Pandey, 1994; Pandey and Sun, 1996) encourages the view that reasonably simple root rotation corrections can indeed restore accuracy. If so, beam theory may be not only useful but even the preferred method, especially for plane problems, including many common experimental tests, since it yields straightforward, relatively small numerical problems and, in many important cases and limits, highly instructive analytical results.

Competition in accurate delamination modeling will come from modern cohesive element methods, which are extensions of finite element formulations to include elements that can introduce bridging and contact tractions in convenient ways. Cohesive models are an attractive, physically based formulation of nonlinear crack tip and crack wake processes, very well suited to complex 3D configurations with arbitrary mode mixtures. They have a growing record of successful simulations of experiments (e.g., Remmers et al., 2003; Yang and Cox, 2004). However, accurate cohesive model analyses of complex laminated structures may comprise 10^6 degrees of freedom and do not yield analytical results, even in limits. Beam theory and computationally intensive cohesive element methods may prove complementary.

6.2. Towards structural design concepts

Many configurations of loads and boundary conditions arise in structures other than the cantilever case studied here. Nevertheless, the cantilever case suggests some principles concerning the role of the multiplicity of delaminations in structural performance that may prove generally applicable to cases of mixed shear and bending.

Assume that residual strength following delamination damage declines as the size of the cracks increases (e.g. Fig. 4). Then the results for uniformly spaced cracks (Eq. (12)) suggest that, to enhance residual strength, material conditions that favour greater number of cracks uniformly distributed through a structure are to be avoided. On the other hand, if the cracks are confined to a band of limited width, then resistance to growth rises with their number. Protection against long cracks might therefore be sought by deliberately introducing multiple weaker planes within a limited band in the material. Of course, the effect of such a strategy on other failure routes must also be considered. For instance by tailoring the material for increased residual strength the ductility of the structure is reduced, leading to a more brittle failure of the structure.

The case study of the system of two cracks shows that interaction effects are strong. Cases in which one crack shields the other and cases in which it leads to accelerated growth in its partner can be found, depending on where the two cracks reside in the laminate. The possibility of acceleration implies that design and life predictions based on solutions for a single crack cannot be safe.

In many cases studied here, the possibility of crack face contact arises. Long zones of crack wake contact and friction can therefore be expected to be common in structural problems involving shear and bending. The friction zones will not generally be confined to a near-tip region, in particular one that is sufficiently small that friction effects could be incorporated by modifying the critical value of the energy release rate. Rather, the friction contact zone will vary in extent (and possibly in the number of contact domains) with the crack size and its relation to other cracks. The contact zones must be calculated explicitly. Similar remarks will apply to treating through-thickness reinforcement, should it be present. Work is in progress to investigate these topics.

7. Conclusions

A model has been presented that allows for the analysis of laminated plates with multiple delaminations deforming in cylindrical bending. The model utilizes the assumptions of classical beam theory, which

neglects shear and near-tip deformation, and accounts for non-frictional contact between the crack surfaces. It has been applied to a cantilever beam with multiple through-width edge delaminations subject to a concentrated load at its free end. Contact has been simulated using different approaches, *unconstrained*-, *constrained*- and *spring-contact*, where the names reflect the approximation used to describe the displacement field. Finite element analyses applied to a two delamination system show that the *spring-contact* model is the most accurate; however utilizing it results in a non-linear problem and thus requires a partially numeric solution while the other models result in closed form solutions. The two simpler approximations give upper and lower bounds of the energy release rate determined by the *spring-contact* approximation. In the case of the mode ratio, however they give results that are often qualitatively different and at times also incorrect. These problems are expected to be compounded in systems of more delaminations with more complicated states of contact. Thus when accurate results are required, the simplified contact approximations should only be used as general bounds and as a first approximation of the regions of contact for the iterative solution of the *spring-contact* model.

Analysis of the energy release rate and mode ratio of the delaminations has revealed several key insights into the behavior of multiply delaminated systems. When delamination growth is considered, a discontinuity in the energy release rate and mode ratio is found when the delaminations reach the same length. This discontinuity leads to instantaneous shielding or amplification of the energy release rate, eliciting behaviors such as local snap-back and snap-through instabilities, hyperstrength, crack pull-along and crack arrest. All of these behaviors are strongly dependent on and controlled by the through-thickness spacing of the delaminations. The energy release rates of the delaminations are also amplified or shielded when the delaminations are not of the same length, again depending on the through-thickness positions of the delaminations. These effects show some similarity to the effects previously observed in the interaction of microcracks or of main cracks with clouds of microcracks in infinite media, which can represent damage in concrete and coarse grain ceramics (Hutchinson, 1987; Rose, 1986; Rubinstein, 1985; Kachanov, 1986; Brencich and Carpinteri, 1996). However in the problem considered here, strong modifications in the results and more complex behaviors are observed due to the finiteness of the structure.

The through-thickness positions of the delaminations also control the sensitivity of a system of equal length delaminations to length perturbations. When the delaminations are equally spaced the equality of length is stable (i.e. simultaneous growth of the delaminations) leading to a more ductile failure; when they are not, the equality of length is often, but not always, unstable resulting in a more brittle response (i.e. growth of one or a limited number of delaminations).

While the present study was limited to a system of only two unequal length delaminations, the proposed model could be applied to analyze systems with a general number of delaminations following the procedure described in Section 2. Behaviors similar to those of the two-delamination system are expected in a system with many delaminations, resulting in a macro structural response with a saw-tooth appearance, with repeated increases and decreases in critical load as the critical delamination tip grows with and past other delamination tips in the system. Different boundary and loading conditions from those studied here are expected to have a mostly quantitative effect on the results and can be easily solved using the same model and solution procedure. With minimal modification, friction acting in the regions of contact can also be considered. Its effect will be additional shielding of the energy release rate at the delamination tips.

Acknowledgements

MGA supported by Northwestern University. RM partially supported by the MIUR-Cofin2004 grant on “Problemi e modelli microstrutturali: applicazioni in ingegneria strutturale e civile” and the US Office of Naval Research through contract no. N00014-05-1-0098, administered by Dr. Yapa D.S. Rajapakse.

BNC supported by the US Army Research Office through contract number DAAD19-99-C-0042, administered by Dr. David Stepp.

Appendix A. Derivation of general solutions for system of coupled differential equations

In this appendix, the general solutions for the system of differential equations, Eqs. (7) and (8) are derived, for one free segment and for 2 and 3 beam segments in contact.

A.1. Single beam segment

For a single beam segment A the governing differential equations, Eqs. (7) and (8), are

$$\begin{aligned} EI_A w_{A,xxxx} &= 0, \\ EA_A u_{A,xx} &= 0 \end{aligned} \quad (\text{A.1})$$

the general solutions of this system of equation is

$$\begin{aligned} w_A(x) &= C_1 + C_2x + C_3x^2 + C_4x^3, \\ u_A(x) &= C_5 + C_6x, \end{aligned} \quad (\text{A.2})$$

where the C 's are unknown constants of integration.

A.2. Two beam segments in contact

For two beam segments A and B in contact, the governing differential equations, Eqs. (7) and (8) are

$$\begin{aligned} EI_A w_{A,xxxx} + k_{A,B}(w_A - w_B) &= 0, \\ EA_A u_{A,xx} &= 0, \\ EI_B w_{B,xxxx} - k_{A,B}(w_A - w_B) &= 0, \\ EA_B u_{B,xx} &= 0, \end{aligned} \quad (\text{A.3})$$

where $k_{A,B}$ is given by Eq. (5). Solutions of the form:

$$w_A(x) = A_1 e^{\kappa x}, \quad w_B(x) = A_2 e^{\kappa x} \quad (\text{A.4})$$

are sought. The resulting algebraic equation, determined by substitution of Eq. (A.4) into Eqs. (A.3) and subsequent elimination of A_1 or A_2 is

$$\kappa^4(\kappa^4 + 4\beta_{A,B}^4)e^{\kappa x} = 0, \quad (\text{A.5})$$

where

$$\beta_{A,B} = \sqrt[4]{\frac{k_{A,B}}{4} \left(\frac{1}{EI_A} + \frac{1}{EI_B} \right)}. \quad (\text{A.6})$$

The relationship between the unknown constants A_1 and A_2 is

$$\frac{A_2}{A_1} = \frac{EI_B}{k_{A,B}} \kappa^4 + 1. \quad (\text{A.7})$$

The 8 roots of Eq. (A.5) are

$$\kappa = 0, 0, 0, 0, \pm(1 \pm i\beta_{A,B}), \quad (\text{A.8})$$

where $i = \sqrt{-1}$. The general solution of this system of differential equations is therefore

$$w_A(x) = EI_A e^{\beta_{A,B}x} (C_1 \cos \beta_{A,B}x + C_2 \sin \beta_{A,B}x) + EI_A e^{-\beta_{A,B}x} (C_3 \cos \beta_{A,B}x + C_4 \sin \beta_{A,B}x) + C_5 x^3 + C_6 x^2 + C_7 x + C_8, \quad (\text{A.9})$$

$$u_A(x) = C_9 + C_{10}x$$

$$w_B(x) = EI_B e^{\beta_{A,B}x} (C_1 \cos \beta_{A,B}x + C_2 \sin \beta_{A,B}x) + EI_B e^{-\beta_{A,B}x} (C_3 \cos \beta_{A,B}x + C_4 \sin \beta_{A,B}x) + C_5 x^3 + C_6 x^2 + C_7 x + C_8 \quad (\text{A.10})$$

$$u_A(x) = C_{11} + C_{12}x.$$

A.3. Three beam segments in contact

The governing differential equations for three beam segments A , B and C in contact are

$$\begin{aligned} EI_A w_{A,xxxx} + k_{A,B}(w_A - w_B) &= 0, \\ EA_A u_{A,xx} &= 0, \\ EI_B w_{B,xxxx} + k_{B,C}(w_B - w_C) &= k_{A,B}(w_A - w_B), \\ EA_B u_{B,xx} &= 0, \\ EI_C w_{C,xxxx} - k_{B,C}(w_B - w_C) &= 0, \\ EA_C u_{C,xx} &= 0. \end{aligned} \quad (\text{A.11})$$

The k 's are given by Eq. (A.5). Solutions of the form

$$w_A(x) = A_1 e^{\kappa x}, \quad w_B(x) = A_2 e^{\kappa x}, \quad w_C(x) = A_3 e^{\kappa x} \quad (\text{A.12})$$

are sought. The resulting algebraic equation for determination of κ is

$$\kappa^4 (\kappa^8 + \alpha_{A,B,C} \kappa^4 + \gamma_{A,B,C}) e^{\kappa x} = 0, \quad (\text{A.13})$$

where

$$\begin{aligned} \alpha_{A,B,C} &= k_{A,B} \left(\frac{1}{EI_A} + \frac{1}{EI_B} \right) + k_{B,C} \left(\frac{1}{EI_B} + \frac{1}{EI_C} \right), \\ \gamma_{A,B,C} &= k_{A,B} k_{B,C} \left(\frac{1}{EI_A EI_B} + \frac{1}{EI_A EI_C} + \frac{1}{EI_B EI_C} \right). \end{aligned} \quad (\text{A.14})$$

The relationships between the unknown constants A_1 , A_2 and A_3 are

$$\begin{aligned} \frac{A_2}{A_3} &= \frac{EI_C}{k_{B,C}} \kappa^4 + 1, \\ \frac{A_1}{A_3} &= \frac{EI_B EI_C}{k_{A,B} k_{B,C}} \kappa^8 + \left(\frac{1}{k_{A,C}} (EI_B + EI_C) + \frac{1}{k_{B,C}} EI_C \right) \kappa^4 + 1. \end{aligned} \quad (\text{A.15})$$

The 12 roots of Eq. (A.13) are

$$\kappa = 0, 0, 0, 0, \pm(1 \pm i) \left(\frac{1}{2} \alpha_{A,B,C} \pm \frac{1}{2} \sqrt{\alpha_{A,B,C}^2 - 4\gamma_{A,B,C}} \right)^{1/4}. \quad (\text{A.16})$$

The general solutions of the system of equations is therefore:

$$\begin{aligned}
 w_A(x) &= C_1 + C_2x + C_3x^2 + C_4x^3 \\
 &\quad + \rho_4 e^{\sqrt[4]{\rho_2}x} (C_5 \sin \sqrt[4]{\rho_2}x + C_6 \cos \sqrt[4]{\rho_2}x) + \rho_3 e^{\sqrt[4]{\rho_1}x} (C_7 \sin \sqrt[4]{\rho_1}x + C_8 \cos \sqrt[4]{\rho_1}x) \\
 &\quad + \rho_3 e^{-\sqrt[4]{\rho_1}x} (C_9 \sin \sqrt[4]{\rho_1}x + C_{10} \cos \sqrt[4]{\rho_1}x) + \rho_4 e^{-\sqrt[4]{\rho_2}x} (C_{11} \sin \sqrt[4]{\rho_2}x + C_{12} \cos \sqrt[4]{\rho_2}x), \\
 w_B(x) &= C_1 + C_2x + C_3x^2 + C_4x^3 \\
 &\quad + \rho_6 e^{\sqrt[4]{\rho_2}x} (C_5 \sin \sqrt[4]{\rho_2}x + C_6 \cos \sqrt[4]{\rho_2}x) + \rho_5 e^{\sqrt[4]{\rho_1}x} (C_7 \sin \sqrt[4]{\rho_1}x + C_8 \cos \sqrt[4]{\rho_1}x) \\
 &\quad + \rho_5 e^{-\sqrt[4]{\rho_1}x} (C_9 \sin \sqrt[4]{\rho_1}x + C_{10} \cos \sqrt[4]{\rho_1}x) + \rho_6 e^{-\sqrt[4]{\rho_2}x} (C_{11} \sin \sqrt[4]{\rho_2}x + C_{12} \cos \sqrt[4]{\rho_2}x), \\
 w_C(x) &= C_1 + C_2x + C_3x^2 + C_4x^3 \\
 &\quad + e^{\sqrt[4]{\rho_2}x} (C_5 \sin \sqrt[4]{\rho_2}x + C_6 \cos \sqrt[4]{\rho_2}x) + e^{\sqrt[4]{\rho_1}x} (C_7 \sin \sqrt[4]{\rho_1}x + C_8 \cos \sqrt[4]{\rho_1}x) \\
 &\quad + e^{-\sqrt[4]{\rho_1}x} (C_9 \sin \sqrt[4]{\rho_1}x + C_{10} \cos \sqrt[4]{\rho_1}x) + e^{-\sqrt[4]{\rho_2}x} (C_{11} \sin \sqrt[4]{\rho_2}x + C_{12} \cos \sqrt[4]{\rho_2}x),
 \end{aligned} \tag{A.17}$$

where

$$\begin{aligned}
 \rho_1, \rho_2 &= \frac{1}{8} \alpha_{A,B,C} \mp \sqrt{\alpha_{A,B,C}^2 - 4k_{A,B}k_{B,C}\gamma_{A,B,C}}, \\
 \rho_3 &= \frac{16EI_BEI_C\rho_1^2}{k_{A,B}k_{B,C}} - 4 \frac{EI_Bk_{B,C} + EI_Ck_{B,C} + EI_Ck_{A,B}}{k_{A,B}k_{B,C}} \rho_1 + 1, \\
 \rho_4 &= \frac{16EI_BEI_C\rho_2^2}{k_{A,B}k_{B,C}} - 4 \frac{EI_Bk_{B,C} + EI_Ck_{B,C} + EI_Ck_{A,B}}{k_{A,B}k_{B,C}} \rho_2 + 1, \\
 \rho_5 &= 1 - \frac{EI_C}{k_{B,C}} \rho_1, \quad \rho_6 = 1 - \frac{EI_C}{k_{B,C}} \rho_2.
 \end{aligned} \tag{A.18}$$

Appendix B. Solutions for n equal length cracks

The solution for the system of n equal length cracks is determined by application of the boundary conditions Eq. (10) and continuity conditions Eq. (11). The general solutions for the intact beam segment, with index $k = 0$, and each of the beam segments, with indices $k = 1, \dots, n + 1$, in the delaminated region using the *unconstrained-contact* model are given by Eq. (A.2):

$$w_k(x) = C_{k,1} + C_{k,2}x + C_{k,3}x^2 + C_{k,4}x^3 \tag{B.1}$$

the $4(n + 1)$ constants of integration are

$$\begin{aligned}
 C_{0,1} &= C_{0,2} = 0, \quad C_{0,3} = \frac{1}{2} \frac{PL}{EI_0}, \quad C_{0,4} = -\frac{1}{6} \frac{P}{EI_0}, \\
 C_{k,1} &= \frac{P}{6} (2a + L)(L - a)^2 \left(\sum_{j=1}^{n+1} \frac{1}{EI_j} - \frac{1}{EI_0} \right), \\
 C_{k,2} &= -\frac{P}{2} (L + a)(L - a) \left(\sum_{j=1}^{n+1} \frac{1}{EI_j} - \frac{1}{EI_0} \right), \\
 C_{k,3} &= \frac{PL}{2} \sum_{j=1}^{n+1} \frac{1}{EI_j}, \quad C_{0,4} = -\frac{P}{6} \sum_{j=1}^{n+1} \frac{1}{EI_j}, \quad k = 1, \dots, n + 1.
 \end{aligned} \tag{B.2}$$

The constants for each of the segments in the cracked region, $C_{k,1}$, $C_{k,2}$, $C_{k,3}$, $C_{k,4}$, are identical, thus the deflections of the beam segments in the cracked region are the same. Therefore the other two contact approximations, the *constrained-contact* and the *spring-contact* yield the same solution.

The solution for the beam with n equal length cracks could also be determined by considering in the cracked region an equivalent intact beam with a reduced bending moment of inertia $I^* = \sum_{j=1}^{n+1} I_j$. This is also true in general under the assumptions of the *constrained-contact* model when the n cracks have arbitrary lengths. In this case, the beam is divided up into segments, each with a reduced bending moment of inertia determined by the sum of the bending moments of inertia of the delaminated sublaminae forming that segment.

The total potential energy Π of the system is

$$\Pi = \frac{1}{6} \frac{P^2 L^3}{EI_0} - \frac{P^2 a^3}{6} \left(\sum_{j=1}^{n+1} \frac{1}{EI_j} - \frac{1}{EI_0} \right). \quad (\text{B.3})$$

Appendix C. Stability analysis of a cantilever beam with n equal length, equally spaced cracks

The stability of the equality of length of n equally spaced cracks in a cantilever beam is analyzed here using the assumptions of the *unconstrained-contact* model. If a positive perturbation Δa of crack m is considered, the energy release rate for crack m is

$$\frac{\mathcal{G}_m E h}{P^2} = 6m(N-m) \left(\frac{a + \Delta a}{h} \right)^2 \left(\frac{\chi_3 a^6 + 6\chi_1 a^3 (a + \Delta a)^3 + 3\chi_2 (a + \Delta a)^6}{\chi_1 a^3 + \chi_2 (a + \Delta a)^3} \right), \quad (\text{C.1})$$

where

$$\chi_1 = 6(m^4 - 2m^3 N + m^2(N^2 - 3) + 3mN - N^2),$$

$$\chi_2 = 3(3m^2 - 3mN + N^2),$$

$$\chi_3 = -\frac{N^4}{3} + \left(\frac{2}{3}\chi_1 + \frac{4}{3}\chi_2 \right) N^2 - \chi_1 \left(\frac{\chi_2}{3} - 3 \right),$$

$$N = n + 1.$$

The energy release rate for each of the remaining $n-1$ cracks is

$$\frac{\mathcal{G}_i E h}{P^2} = 6 \frac{N^2}{N-2} \left(\frac{a}{h} \right)^2 \left(\frac{\chi_4 a^6 + \chi_5 a^3 (a + \Delta a)^3 + \chi_6 (a + \Delta a)^6}{\chi_1 a^3 + \chi_2 (a + \Delta a)^3} \right), \quad (\text{C.2})$$

where

$$\chi_4 = \chi_1 \left(-\frac{1}{3}N^2 + \frac{1}{3}\chi_2 + \chi_1 + 1 \right),$$

$$\chi_5 = -\frac{2}{3}N^2(N^2 - \chi_2) + 2(\chi_2 + \chi_1\chi_2 + 3\chi_1),$$

$$\chi_6 = -\frac{2}{3}N^2 \left(N^2 - \frac{5}{2}\chi_2 \right) + 4\chi_2 + 5\chi_1.$$

The ratio of energy release rates, Eq. (C.1) by Eq. (C.2), taking the limit as $\Delta a \rightarrow 0$ is

$$\frac{\mathcal{G}_m}{\mathcal{G}_i} = \frac{m(N-m)(N-2)}{N^2} \left(\frac{\chi_3 + 6\chi_1 + 3\chi_2}{\chi_4 + \chi_5 + \chi_6} \right) = \frac{(n^2 - mn + 2n - m + 1 + m^2)(n-1)}{(-m^2 + mn + m - 1)(n+1)^2}. \quad (\text{C.3})$$

The equality of length is stable if, for $n \geq 2$, $\mathcal{G}_m/\mathcal{G}_i < 1$. This condition is checked by verifying it at the extremum in terms of m and at the boundaries for $m = 1, n$. This yields

$$\frac{\mathcal{G}_{m_{\text{ext}}}}{\mathcal{G}_i} = \frac{3}{n+3}, \quad \frac{\mathcal{G}_1}{\mathcal{G}_i} = \frac{\mathcal{G}_n}{\mathcal{G}_i} = 1 - \frac{n}{(n+1)^2} \quad (\text{C.5})$$

which are always less than 1 for $n \geq 2$.

If a negative perturbation Δa of crack m is considered then the energy release rate for crack m is

$$\frac{\mathcal{G}_m E h}{P^2} = \left(\frac{a - \Delta a}{h} \right)^2 \frac{144N^2 a^6}{(3(N-2)(a - \Delta a)^3 + (N+6)a^3)^2}. \quad (\text{C.6})$$

The energy release rate for each of the remaining $n-1$ cracks is

$$\frac{\mathcal{G}_i E h}{P^2} = 6 \left(\frac{a}{h} \right)^2 \frac{\chi_7 [(N+6)a^6 + 6(N-2)a^3(a - \Delta a)^3] + 9\chi_8(a - \Delta a)^6}{(3(N-2)(a - \Delta a)^3 + (N+6)a^3)^2}, \quad (\text{C.7})$$

where

$$\begin{aligned} \chi_7 &= (N^2 + 2N + 3), \\ \chi_8 &= (N^3 - N + 2). \end{aligned}$$

The ratio of energy release rates, Eq. (C.6) by Eq. (C.7), taking the limit as $\Delta a \rightarrow 0$ is

$$\frac{\mathcal{G}_m}{\mathcal{G}_i} = \frac{144N^2}{\chi_7(7N+6) + 9\chi_8} = \frac{3n+3}{2n+3}. \quad (\text{C.8})$$

The equality of length is stable if, for $n \geq 2$, $\mathcal{G}_m/\mathcal{G}_i > 1$, which clearly is satisfied by Eq. (C.8). Thus the equality of length is stable for n equally spaced cracks.

Appendix D. Energy release rate expressions for a cantilever beam with two delaminations

The expressions for the normalized energy release rate for the upper and lower delamination, \mathcal{G}_U and \mathcal{G}_L for the cantilever beam of Fig. 5 are presented here. When the upper delamination is longer than the lower, $a_U > a_L$ Fig. 5a, the solution shows that there is contact along the delamination surfaces. The normalized energy release rates for the upper and lower delamination have been determined in closed form for the *unconstrained*- and *constrained-contact* models. The energy release rate for the *spring-contact* model is determined through the numerical solution of the problem and application of Eq. (9a).

For the *constrained-contact* model the energy release rates for $a_U > a_L$ are

$$\frac{\mathcal{G}_U E h}{P^2} = 18 \left(\frac{a_U}{h} \right)^2 \left(\frac{H_3(1-H_3)}{3H_3^2 - 3H_3 + 1} \right), \quad (\text{D.1})$$

$$\frac{\mathcal{G}_L E h}{P^2} = 18 \left(\frac{a_L}{h} \right)^2 \left(\frac{H_5(1-H_3)(1-H_3-H_5)}{(3H_3^2 - 3H_3 + 1)(1 - 3(H_3 + H_5)(H_5H_3 + 1) + 3(H_3 + H_5)^2)} \right), \quad (\text{D.2})$$

where $H_3 = h_3/h$ and $H_5 = h_5/h$. For the *unconstrained-contact* model the energy release rates for $a_U > a_L$ are

$$\frac{\mathcal{G}_U Eh}{P^2} = 18 \left(\frac{a_U}{h} \right)^2 \left(\frac{H_3(1-H_3)(\gamma_1(a_U/h)^6 + \gamma_2(a_U/h)^3(a_L/h)^3 + \gamma_3(a_L/h)^6)}{(\gamma_4(a_U/h)^3 + \gamma_5(a_L/h)^3)^2} \right), \quad (D.3)$$

$$\frac{\mathcal{G}_L Eh}{P^2} = 18 \left(\frac{a_L}{h} \right)^2 \left(\frac{(a_U/h)^6 H_5(1-H_3)^3(1-H_3-H_5)\gamma_6}{(\gamma_4(a_U/h)^3 + \gamma_5(a_L/h)^3)^2} \right), \quad (D.4)$$

where the constants $\gamma_1, \dots, \gamma_6$ depend on the through-thickness positions of the cracks and are

$$\begin{aligned} \gamma_1 &= (3H_3^2 - 3H_3 + 1)(H_3^2 + 3H_5^2 + 3H_3H_5 - 2H_3 - 3H_5 + 1)^2, \\ \gamma_2 &= 6H_5H_3^3(1-H_3-H_5)(H_3^2 + 3H_5^2 + 3H_3H_5 - 2H_3 - 3H_5 + 1), \\ \gamma_3 &= 3H_5^2H_3^2(1-H_3-H_5)^2(H_3^2 + H_3 + 1), \\ \gamma_4 &= -(3H_3^2 - 3H_3 + 1)(H_3^2 + 3H_5^2 + 3H_3H_5 - 2H_3 - 3H_5 + 1), \\ \gamma_5 &= -3H_5H_3^3(1-H_3-H_5). \end{aligned} \quad (D.5)$$

When the lower delamination is longer than the upper delamination, $a_L > a_U$ Fig. 5b, the solution shows that there is opening along the lower delamination face, and no contact along the upper delamination face, namely the two upper beam segments have the same vertical deflection. Therefore, the *spring-* and *unconstrained-contact* models lead to the same solution. The *constrained-contact* model, which prevents opening, leads to a solution that is clearly incorrect in this regime. However, as will be seen later, it is a bound of the exact solution, which is useful for delamination configurations with more delaminations where the exact solution is not so obvious. The energy release rates are given by Eqs. (D.1)–(D.5) with the indices of crack positions and lengths reversed, $a_L \rightarrow a_U$, $a_U \rightarrow a_L$, $H_3 \rightarrow H_5$ and $H_5 \rightarrow H_3$.

When the delaminations have the same length, the energy release rate of each delamination when the delaminations propagate simultaneously, \mathcal{G}_B , is given by Eq. (12).

As for the case of equal length delaminations, Fig. 3, maps can be constructed for a general through-thickness distribution and lengths of the delaminations that show regions in which the energy release rate

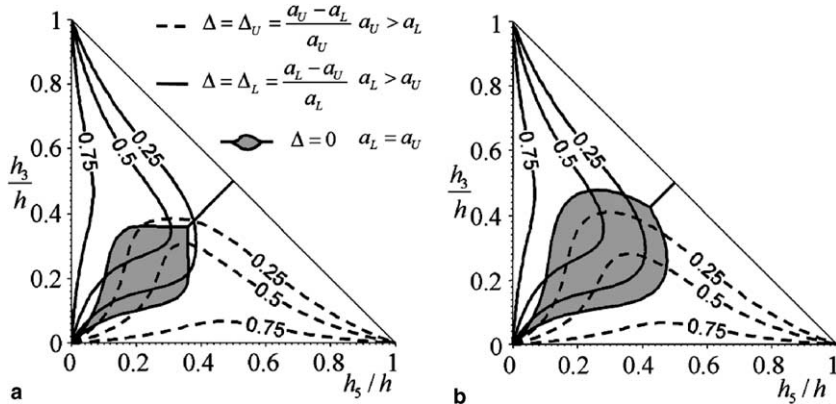


Fig. D.1. Maps of regions of different energy release rates for a system of two unequal length cracks (schematic of Fig. 5): (a) unconstrained model, (b) constrained model.

of one of the cracks is higher or lower than that of the other crack. Maps for the *constrained*- and *unconstrained-contact* models are shown in Fig. D.1.

The maps depend on the through-thickness position of the two cracks and incorporate contours of equal \mathcal{G} of both cracks. The contours depend on the relative length of the two cracks. Dashed contours correspond to $\Delta_U = (a_U - a_L)/a_U$ and are to be used when $a_U > a_L$. Solid contours correspond to $\Delta_L = (a_L - a_U)/a_L$ and are to be used when $a_L > a_U$. The map in Fig. D.1a has been constructed using the *unconstrained-contact* model and the map in Fig. D.1b using the *constrained-contact* model. A more complicated map, depending also on the length of the cracks, can be constructed using the *spring-contact* model.

The shaded region in each figure refers to cracks of the same length, $\Delta_U = \Delta_L = 0$, and define configurations for which the energy release rate of each crack when the cracks propagate simultaneously, \mathcal{G}_B given by Eq. (12), is maximum (the shaded region in Fig. D.1a coincides with that of Fig. 3). Points to the left or above the contour corresponding to the relative length of the two cracks define through-thickness distributions of the cracks for which the upper crack has the higher energy release rate. Points below or to the right of the contour define through-thickness distributions of the cracks for which the lower crack has the higher energy release rate. The evolution of the cracks can be followed in this diagram by updating the contour from that corresponding to the current Δ , to the configuration reached by the last crack growth event.

References

- Andrews, G.M., Massabò, R., Cox, B.N., 2005. Frictional Interaction of Multiple Delaminations with Shear and Near Crack-Tip Deformation, Internal Report, University of Genova, Italy.
- Brenchich, A., Carpinteri, A., 1996. Interaction of a Main Crack with Ordered Distributions of Microcracks: A Numerical Technique by Displacement Discontinuity Boundary Elements. *Int. J. Fracture* 76 (4), 373–389.
- Chan, S.K., Tuba, I.S., Wilson, W.K., 1970. On the finite element method in linear fracture mechanics. *Eng. Frac. Mech.* 2 (1), 1–17.
- Hutchinson, J.W., 1987. Crack tip shielding by microcracking in brittle solids. *Acta Metallurgica* 35 (7), 1605–1619.
- Hutchinson, J.W., Suo, Z.G., 1992. Mixed-Mode Cracking in Layered Materials. *Adv. Appl. Mech.* 29, 63–191.
- Kachanov, M., 1986. On Crack–Microcrack Interactions. *Int. J. Fracture* 30 (4), 65–72.
- Kanninen, M.F., 1973. Augmented double cantilever beam model for studying crack propagation and arrest. *Int. J. Fracture* 9 (1), 83–92.
- Kanninen, M.F., 1974. Dynamic analysis of unstable crack propagation and arrest in the DCB test specimen. *Int. J. Fracture* 10 (3), 415–430.
- Kerr, A.D., 1964. Elastic and Viscoelastic Foundation Models. *J. Appl. Mech.* 31, 491–498.
- Larsson, P.L., 1991. On Multiple Delamination Buckling and Growth in Composite Plates. *Int. J. Solids Structures* 27 (13), 1623–1637.
- Li, S., Wang, J., Thouless, M.D., 2004. The effects of shear on delamination in layered materials. *J. Mech. Phys. Solids* 52 (1), 193–214.
- Massabò, R., Cox, B.N., 1999. Concepts for Bridged Mode II Delamination Cracks. *J. Mech. Phys. Solids* 47 (6), 1265–1300.
- Pandey, R.K., Sun, C.T., 1996. Calculating strain energy release rate in cracked orthotropic beams. *Journal of Thermoplastic Composite Materials* 9 (4), 381–395.
- Pavier, M.J., Clarke, M.P., 1995. Experimental-technique for the investigation of the effects of impact damage on carbon-fiber composites. *Composite Science and Technology* 55 (2), 157–169.
- Remmers, J.J.C., de Borst, R., Needleman, A., 2003. A cohesive segments method for the simulation of crack growth. *Computational Mechanics* 31 (1–2), 69–77.
- Rice, J.R., 1968. A Path Independent Integral and Approximate Analysis of Strain Concentration by Notches and Cracks. *J. Appl. Mech.* 35 (2), 379–386.
- Rose, L.R.F., 1986. Microcracking interaction with a main crack. *Int. J. Fracture* 31 (3), 233–242.
- Rubinstein, A.A., 1985. Macrocrack interaction with semi-infinite microcrack array. *Int. J. Fracture* 27 (2), 113–119.
- Sridhar, N., Massabò, R., Cox, B.N., Beyerlein, I., 2002. Delamination Dynamics in Through-Thickness Reinforced Laminates with Application to DCB Specimen. *Int. J. Fracture* 118, 119–144.
- Suemasu, H., 1993. Postbuckling Behaviors of Composite Panels with Multiple Delaminations. *J. of Compos. Mater.* 27 (11), 1077–1096.
- Suemasu, H., Majima, O., 1996. Multiple Delaminations and Their Severity in Circular Axisymmetric Plates Subjected to Transverse Loading. *J. of Compos. Mater.* 30 (4), 441–463.

- Sun, C.T., Pandey, R.K., 1994. Improved method for calculating strain energy release rate based on beam theory. *AIAA Journal* 32 (1), 184–189.
- Suo, Z.G., 1990. Delamination Specimens for Orthotropic Materials. *J. Appl. Mech.* 57 (3), 627–634.
- Suo, Z.G., Hutchinson, J.W., 1990. Interface crack between two elastic layers. *Int. J. Fract.* 43 (1), 1–18.
- Wang, J., Qiao, P., 2004. Interface crack between two shear deformable elastic layers. *J. Mech. Phys. Solids* 52, 891–905.
- Williams, J.G., 1989. End Corrections for Orthotropic DCB Specimens. *Composite Science and Technology* 35 (4), 367–376.
- Yang, Q.D., Cox, B.N., 2004. Modeling damage evolution in laminated composites containing stress concentrators, *International Journal of Solids and Structures* in preparation for submission.
- Zheng, S., Sun, C.T., 1998. Delamination Interaction in Laminated Structures. *Eng. Frac. Mech.* 59 (2), 225–240.



Dynamic Fiber Sliding along Debonded, Frictional Interfaces

Q. D. Yang,¹ A. Rosakis,² and B. N. Cox¹

¹ Rockwell Scientific
1049 Camino Dos Rios
Thousand Oaks, CA
U.S.A.

² Department of Aeronautics
California Institute of Technology
Pasadena, CA
U.S.A.

Submitted to
The Proceedings of the Royal Society
April 22, 2005; revised, September, 2005

ABSTRACT

The problem is considered of a fiber that is driven dynamically, by compression at one end, into a matrix. The fiber is not initially bonded to the matrix, so that its motion is resisted solely by friction. Prior work based on simplified models has shown that the combination of inertial effects and friction acting over long domains of the fiber-matrix interface give rise to behaviour that is far more complex than in the well-known static loading problem. The front velocity may depart significantly from the bar wave speed and regimes of slip, slip/stick, and reverse slip can exist for different material choices and loading rates. Here more realistic numerical simulations and detailed observations of dynamic displacement fields in a model push-in experiment are used to seek more complete understanding of the problem. The prior results are at least partly confirmed, especially the ability of simple shear lag theory to predict front velocities and gross features of the deformation. Some other fundamental aspects are newly revealed, including oscillations in the interface stresses during loading; and suggestions of unstable, possibly chaotic interface conditions during unloading. Consideration of the experiments and two different orders of model suggest that the tentatively characterized chaotic phenomena may arise because of the essential nonlinearity of friction, that the shear traction changes discontinuously with the sense of the motion, rather than being associated with the details of the constitutive law that is assumed for the friction. This contrasts with recent understanding of instability and ill-posedness at interfaces loaded uniformly in time, where the nature of the assumed friction law dominates the outcome.

1. Introduction

This paper will address certain aspects of the more general problem illustrated in Figure 1. In the general problem, a fiber that is initially bonded to a matrix is loaded dynamically in either tension or compression at its end, with a load that is some function of time. The fiber and matrix are elastically dissimilar. The assembly may be of plane or axisymmetric geometry. Boundary conditions for the axisymmetric case may be those of Type I or Type II (i.e., stress or displacement conditions at the boundary of a cylindrical cell), as designated by Hutchinson and Jensen (Hutchinson and Jensen, 1990) to simulate an array of fibers; or those corresponding to an isolated fibre in a semi-infinite body. Boundary conditions for a plane problem may be periodic to simulate an array; or again those of an isolated fiber in a semi-infinite body. A state of initial compression may exist across the fiber-matrix interface, e.g., due to residual thermal stresses. The load causes the fiber to debond progressively from the matrix, allowing relative sliding between the two, which is opposed by friction. The constitutive law of the friction may involve displacement, displacement rate, and the magnitude of the interface compression. The debonding mechanism may result in a nonlinear process zone in the debond crack wake of significant length. Friction will generally act over much longer lengths, often the whole domain of sliding.

In this paper, model experiments and numerical simulations of the push-in problem (compressive end loading) will be used to study the particular limit that the interface is initially debonded (limit of zero debond toughness). One motivation is to explore the connections between the physics of long range frictional sliding and shear fracture, using model experiments in which a reduced set of mechanisms operates. Simultaneously, the question is addressed of how simply dynamic interface failure in composites can be represented, without loss of accuracy. The latter query is inspired by watershed experiments in the static case on cylindrical fibers in a matrix (e.g., (Marshall, 1992)). In the static case, shear lag analysis of the fiber/matrix debonding problem, which assumes Lamé-like field solutions, proves very accurate for most parameter ranges (Hutchinson and Jensen, 1990) and forms an immediate link to the problem of composite fracture (Budiansky *et al.*, 1986; Marshall *et al.*, 1985). Where static shear lag models are accurate, analytical results usually stand independently of whether the fibers are more or

less compliant than the matrix and whether plane or axisymmetric conditions exist; preliminary shear lag analyses of the dynamic case suggest the same compass, although the physics are considerably more complicated than in the static case (Sridhar *et al.*, 2003). The problem of Fig. 1 may also be considered as a particular case of delamination failure in a symmetrically laid up laminated composite, for which the plane geometry is directly applicable and the lamina represented by the fiber may be more or less compliant than the other layers. The questions of how accurate shear lag theory might be in dynamic cases, and what subset of the physics of interface failure might remain reasonably well represented in it, are therefore of practical interest. Issues specific to the push-in problem will be addressed here, including how the degrees of freedom used in representing displacement fields in modeling and the assumed nature of the friction law influence stability, front formation, front velocity, stress fields, etc.

Friction Acting Along Bars

Shear-lag models of the dynamic case of the problem of Fig. 1, with friction that is spatially and temporally uniform in magnitude (but not in sign), have revealed the regimes of behaviour that might be expected for an initially debonded interface (Cox *et al.*, 2001; Nikitin and Tyurekhodgaev, 1990; Sridhar *et al.*, 2003). First, the front of the furthest deformation in the fiber does not travel at the longitudinal wave speed for the fiber, C_f , but at some other velocity that depends on the friction strength, the elastic mismatch, the wave speeds in the fiber and the matrix, and the loading rate. The front velocity is bounded by C_f and the longitudinal wave speed in the matrix, C_m , and may be lower or higher than C_f . Second, depending on the same parameters, distinct regimes of slip, slip and stick, and reverse slip exist, even when the load point displacement is monotonic. Reverse slip refers to the condition that the relative motion of the fiber and matrix is opposite in sense to that of the load point. Reverse slip is possible when the wave speed in the matrix is higher than that in the fiber, so that the fiber is pulled along, at the deformation front, by the matrix. The domains of slip, stick, and reverse slip are fixed (growing similarly with time) for linearly increasing loads, but appear and disappear in complicated sequences for other loading cases, even those that are simple functions of time (e.g., step functions). The solutions are much more complicated than for the same problem in static loading, where the only history dependence that affects the

solution is the order of any load reversals [e.g., (Marshall, 1992)]. There is even a hint (unproven) that the birth and death of slip, reverse slip, and stick-slip domains may be chaotic, with arbitrarily small changes in the load point history resulting, at later times, in finitely dissimilar domain patterns. Numerical work has supported the shear lag results for linearly increasing loading, under the modeling conditions assumed, for most parameter values (Sridhar *et al.*, 2003). However, the strong non-linearity of the friction law, which may reverse sense at moving boundaries, makes accurate numerical location of the boundaries very challenging, even under the constraint of assumed Lamé-like solutions (Sridhar, Dunn, and Cox, unpublished work, 2002).

Friction Between Half-Spaces

The problem of an interface with no debond energy but long, possibly infinite, domains of friction has been studied extensively in the geometry of two remotely and uniformly loaded half-spaces, contacting on a plane. Among a number of insightful articles, the introductory sections of (Cochard and Rice, 2000) provide an especially helpful summary. Some salient results are as follows. 1) For elastically dissimilar materials subject to Coulomb friction, uniform slip becomes unstable and slip pulses can form instead, i.e., slip domains on either side of which the interface is not sliding (Adams, 1998; Weertman, 1980). Slip pulses can propagate in either direction, in different cases, and at values of the remote shear stress that are less than the friction stress. 2) Unstable slip is also possible for elastically homogeneous cases, but not for a simple Coulomb law. 3) Cochard and Rice go on to distinguish instability from ill-posedness: the former exists when spatial perturbations to the state of slip grow in amplitude; the latter refers to the non-existence of solutions of any kind. Instability does not preclude the possibility of uniform slip as a formal solution, given the hypothetical presence of perfectly uniform conditions. Ill-posedness points to an inconsistency in the physics of the problem as stated. 4) Whether the interface problem exhibits ill-posedness or instability depends on both the degree of elastic mismatch and the nature of the assumed friction law. The relevant measure of elastic mismatch is the point at which the generalized Rayleigh velocity (a mode of interface wave propagation found for a frictionless interface along which loss of contact does not occur) ceases to be defined. Ill-posedness prevails for all friction coefficients when the elastic mismatch is mild (generalized Rayleigh wave

exists); and for friction coefficients above a modest critical value when the mismatch is more severe. Thus ill-posedness is the common case. 5) Ranjith and Rice (Ranjith and Rice, 2001) assign blame to the simplified physics of Coulomb's law, in particular its implication that friction can change discontinuously in time upon a finite change in the normal contact pressure. A modified law, in which the change occurs smoothly over a characteristic response time, had in fact already been inferred from experiments (Prakash and Clifton, 1993; Prakash, 1998). Such a law regularizes the ill-posed planar interface problem; and the regularized solutions continue to exhibit slip-pulse character (Cochard and Rice, 2000).

The complexity seen in the Lamé-like solutions to the push-in problem of Fig. 1 has different physical origins to the instability and ill-posedness discussed in the last two paragraphs. In the work based on Lamé-like solutions, the friction force was assumed to be uniform and constant, apart from sign reversals, and not influenced by changes in the normal compression at the interface. Complexity arises from the effects of friction on the propagation of wave pulses along the fiber and matrix system, excited by the dynamic end loading, and is associated with the birth and death of slip, stick, and reverse slip domains, which is complicated by the strength of the nonlinear effects due to the sign-reversal property of the friction. In the problem of planar frictional interface between half-spaces, instability and ill-posedness are direct consequences of the assumed relation between friction and the normal traction, and depend strongly on whether Coulomb's or another law is assumed.

The final point from the body of work on planar interfaces that is of present relevance is the relation of the boundedness of slip-pulse domains to the nature of the assumed friction law. Zheng and Rice (Zheng and Rice, 1998) looked at this question with a velocity-weakening friction law, expressed as a decrease in the coefficient of friction as the shear displacement rate rises. (This law is similar to that of Prakash and Clifton, but expressed in inverse form, in terms of the displacement rate rather than the rate of change of the shear traction.) For such a law, slip motion can occur either as a crack-like event, in which the interface slips simultaneously over a semi-infinite domain extending back from a slip front; or as a slip-pulse motion, with slip confined to finite, moving domains. Which case prevails (in the problem of contacting half-spaces) depends on the rate of

velocity weakening: if the slope of the decline is small, crack-like slip behaviour occurs; if it is large, slip-pulse motion occurs (Zheng and Rice, 1998).

Effects of Interface Bonding

A separate, major body of literature has been written on the problem of interface shear crack propagation in systems in which the interface is initially bonded. The most pertinent results here refer to the question of allowed and preferred crack velocities. Energy considerations suggest that, unlike mode I cracks, which are forbidden above the shear wave speed, shear cracks can in principle propagate at any velocity, c , in the so-called intersonic regime, $C_S < c < C_L$, where C_S and C_L are the shear and longitudinal wave speeds (Broberg, 1994; Burridge *et al.*, 1979). However, numerical studies imply a restrictive condition for intersonic propagation, that the crack tip process zone be diffused over a finite interval and not concentrated at a point, as in a classical brittle crack (Andrews, 1976). In the work of Burridge *et al.*, the velocity $\sqrt{2}C_S$ assumes a special role: for $c < C_S$, crack acceleration is unstable (associated with decreasing load); while for $c > \sqrt{2}C_S$, crack acceleration is stable (increasing load).

These early theoretical deductions have now been complemented by experiments that have achieved shear crack conditions for the first time in the laboratory by exploiting the propensity of laminated materials to confine cracks to prescribed planes (Rosakis *et al.*, 1999). Specimens consisting of monolithic slabs laminated at a bonded interface as well as composite ply laminates have been studied. Under appropriate dynamic loading, approximately mode II conditions can be maintained, in contrast to tests with a uniform body (free of pre-existing weak planes), where crack deflection or bifurcation would quickly cause a transition to mode I conditions. The laminate experiments confirm mode II crack propagation in the intersonic regime and are also consistent with the predicted stability transition at $\sqrt{2}C_S$, since the crack is observed to accelerate rapidly past the shear wave speed, but decelerate and achieve approximately uniform velocity at $\sqrt{2}C_S$. Needleman has performed numerical simulations of this particular experimental configuration, where the driving force is a dynamic impact end-load rather than the remote shear loading of the early theoretical studies, and confirmed most aspects of the observed behaviour (Needleman, 1999). Needleman's model incorporates mixed mode

cohesive elements to represent the debonding process, with cohesive laws (traction vs. displacement) that feature both an initial hardening phase and a decaying tail. These laws are somewhat different from that in Burrridge *et al.*, which was a purely softening law and for mode II displacements only. The details of the law do affect the outcome in some ways. For example, while Needleman's simulations show the same qualitative history of rapid acceleration to a nearly constant velocity as seen in experiments (Rosakis *et al.*, 1999), the value of the final velocity generally exceeds $\sqrt{2}C_S$, rather than equalling it, with the speed attained depending on the maximum stress assumed for the cohesive law. In a separate theoretical study of shear crack propagation along bi-material (Homalite/steel) interfaces, a large jump in terminal crack velocity was found at a certain prescribed load point velocity (Needleman and Rosakis, 1999). For inferior load point velocities, crack propagation was limited by the Rayleigh wave speed in the Homalite (the slower medium); above the transition, the terminal velocity approximately doubled, to be near the longitudinal wave speed of the Homalite.

While intersonic propagation is physically admissible, shear crack propagation remains forbidden in the velocity interval, $C_R < c < C_S$, where C_R is the Rayleigh velocity. The mechanism by which a crack can jump across this velocity gap involves the creation of a daughter crack ahead of the parent crack, which then links to the parent in an effective surge of crack growth (Andrews, 1976; Burrridge, 1973; Gao *et al.*, 2001). While relationship of this phenomenon to slip-pulse solutions for planar frictional interfaces must exist, the presence of a velocity gap must be associated with presence of concentrations of tractions where interface debonding is taking place, which do not generally appear in interfaces coupled solely by friction.

Contrasts in Physics

Thus shear crack propagation analysis, pulse-slip solutions for the planar frictional interface, and Lamé-like solutions of the push-in problem with zero debond energy (Fig. 1) all show that variable front velocities up to the maximum of the longitudinal wave speeds in the fiber and the matrix are physically admissible. However, important distinctions arise between the different problems. In particular, there is no analogue in the Lamé-like solutions of the push-in problem with zero debond energy to the velocity

gap in the interval (C_R , C_S) in fracture problems, nor any special role for the velocity $\sqrt{2}C_S$. Neither do direct analogues of the phenomena of instability and ill-posedness that have been so extensively studied for planar frictional interfaces appear in the existing Lamé-like solutions, since these have been developed for uniform and constant (not Coulomb) friction.

Solutions in the literature for dynamic shear cracks and the initially-debonded push-in problem also differ in another very important way. Even though cohesive models have been used for dynamic shear crack modeling, thus spreading the debond process into a diffuse process zone, the dimensions of this process or cohesive zone have been relatively small. For example, in the simulations of Needleman (Needleman, 1999), the cohesive zone is ~ 1 mm (a result of the assumed parameter values in the cohesive law), while the crack propagates over distances of ~ 25 mm. Behind the cohesive zone, the fracture surfaces remain traction free. A small process zone representing debonding is very different from the conditions expected in the presence of friction, especially in mode II problems, where shear tractions may act over the whole cracked specimen. While a shear cohesive traction enters the fracture problem in exactly the same way that a frictional traction would enter, the extension of cohesive modeling to friction zones that may be as long as the crack has not been made in dynamic fracture studies. (Calculations for bi-material interfaces did predict the existence of large-scale contact zones trailing the crack-tip (Needleman and Rosakis, 1999), but friction in these zones was not modelled.) Models have either treated long zones of friction in the absence of a debond process (the Lamé-like push-in problem or the planar frictional interface problem); or debonding as a relatively short process zone in the absence of long zones of friction.

Final introductory comments are directed upon the nature of the cohesive law. In static fracture of a material that is not rate dependent, only two or three degrees of freedom in the cohesive law have a significant influence on the fracture response (e.g., (Bao and Suo, 1992; Cox and Marshall, 1994; Massabò and Cox, 1999)). If the zone has finite extent, most characteristics of crack propagation are determined by two parameters, which may be taken as the critical traction in the cohesive law and the area under the law (work of fracture). If the cohesive law incorporates an initial hardening phase (traction rising with

displacement), then the cohesive mechanism may act over the whole crack, even for very long cracks, in which case a third parameter, the slope of the hardening phase, controls crack growth (Cox and Marshall, 1994). If the cohesive mechanism exhibits rate dependence (excluding inertial effects), e.g., due to creep or viscosity, then one or at most two additional parameters, describing the rate of decay of the cohesive tractions, appear to suffice to predict fracture behaviour (Cox and Sridhar, 2001). The possibilities when inertial effects enter may be richer. For example, in none of the work on static fracture are there cases where the rate of decline of the law with increasing displacement plays a significant role (except as it affects the area under the curve, i.e., the work of fracture). Yet in dynamic studies of friction, the rate of decline of the coefficient of friction, i.e., of the cohesive shear traction due to friction, with displacement rate has a profound effect: it determines whether slip occurs in a crack-like or slip-pulse mode (Zheng and Rice, 1998). This and other results, including theoretical models (Lapusta and Rice, 2003) and novel laboratory simulations of slip-pulse motion (Xia *et al.*, 2004), show that constitutive laws for dynamic friction need to be represented with more degrees of freedom than laws in static fracture. Inertial effects appear to manifest further details of the traction law in fracture behaviour.

All of these background works have addressed some aspects of the general problem of Fig. 1, but they remain separate pieces of understanding, not yet connected to one another. Thus large-domain friction problems have not yet embraced the influence of a strong bond (energetically significant crack tip process); while fracture work has not yet extended to very large (possibly semi-infinite) domains of friction. Generality in the friction law has begun to appear only in studies devoted to friction as a phenomenon, but these studies imply that over-simplifying friction laws can have a strong affect on the possible behaviour in other systems. And last, the most general studies of fiber push-in as a special problem, with general end-loading histories, remain to be undertaken.

2. Experiments

A model planar specimen geometry was designed to investigate dynamic fiber push-in for a bi-material system in which no chemical bond exists at the material interface. A transparent and birefringent polymer sheet (Homalite-100), acting as a “fiber,” was placed between two steel plates, analogous to a “matrix” (Fig. 2). The dynamic fiber

push-in process was mimicked by loading the fiber with a projectile traveling at speeds ranging from 10 to 40 m/sec. The resistance of the polymer/metal interfaces to slip was manipulated by applying a static compressive pre-load acting perpendicular to the interfaces, whose value varied from 0.5 – 175 MPa.

Discussion of the resulting deformation will refer to the coordinate system, (x_1, x_2) , with the origin located at the mid-plane of the Homalite piece, at the end where it is impacted (Figs. 1 and 2). The half-height of the Homalite will be denoted h . Thus the interfaces lie at $x_2 = \pm h$. The origin of time, t , is the moment of first impact.

Materials and Specimens: The densities and relevant wave speeds of the test materials are given in Table 1. All plates were 9.5 mm thick and 82.5 mm in length. The steel pieces were 50.8 mm in height. The height, $2h$, of the Homalite piece was 16.5 mm. The Homalite dimensions were chosen to provide a fiber aspect ratio, defined as length divided by the half height, h , of 10. The steel height was chosen to minimize the interactions of wave reflections from the specimen boundaries with the dynamic sliding process. This assures that the case studied is equivalent to that of an isolated fiber in a semi-infinite body. The pieces of the specimen were aligned and stacked vertically (steel/Homalite/steel) without the use of adhesive or bonding agent.

Table 1. Density and elastic wave speeds for the test materials

	density, ρ (kg/m ³)	C_R (m/s)	C_S (m/s)	C_L (m/s)
Homalite	1230	1087	1187	2060
steel	8000	2977	3254	5443

Dynamic Loading and Characterization: The fiber was loaded dynamically by impacting its end with a 25.4 mm diameter cylindrical steel projectile, 44.5 mm in length, which was accelerated using a light air gun. Projectile speeds were varied over the range 10 – 40 m/s by varying the gun pressure. A small steel tab was affixed to one end of the Homalite piece to eliminate the possibility of impact damage to the end of the relatively brittle polymer during dynamic loading (Fig. 2). The dynamic sliding of the Homalite

relative to the steel was characterized using high-speed photography in conjunction with dynamic photoelasticity. A strain gage was mounted to the surface of the steel tab to provide a trigger signal for the initiation of the recording of high-speed photographs (described below). From sequences of images, the dynamic loading history, $\sigma(t)$, of the fiber, the initiation time for the onset of interface sliding, and the interface slip speed histories were obtained.

Dynamic photoelasticity apparatus was configured as follows. A collimated laser beam, 100 mm in diameter, was passed through a circular polarizer, the length of the Homalite, and a second polarizer to generate the photoelastic images, which were recorded using a high-speed digital camera (Cordin 220-16, Cordin Scientific Imaging, Salt Lake City, Utah, 84119). The camera was capable of recording 16 frames. The frames were recorded every few microseconds; the interframe times were varied in each experiment. In dynamic photoelasticity, the fringes show constant-value contours of the difference of principal stresses, $\sigma_1 - \sigma_2$.

2.1 Results

General observations:

A total of 16 experiments were conducted. The role of impact speed (loading rate) was investigated at a constant static pre-load; and that of pre-load was investigated at a constant impact speed. Figure 3 shows a representative high-speed isochromatic fringe pattern recorded during sliding in the common member of these two test sets ($\sigma_{22}^{(r)} = 50$ MPa, $v_0 = 38 \pm 2$ m/s). The approximately vertical fringes represent the stress generated from the impact (from the left) and propagate to the right. Shortly behind the propagating front, kinks form in the fringes in angled bands. These bands intersect the top and bottom interfaces, implying non-smooth variations in the interface displacement. Among the many fringe patterns collected from all tests, consistency in the pattern of bands was imperfect. In some images, either noise or experimental variance made it difficult to confirm or refute the presence of bands that might have been expected to be present based on their presence in other images. In the images with better-defined fringes, two bands were prominent, typified by the dashed white lines in Fig. 3. Based on changes in the spacing or angle of fringes before and after a band, or in the derivative of the spacing,

the first of these is interpreted as the beginning of a domain of increasing interface shear stress; the second as the point of transition to interfacial sliding. In Fig. 3, the domain marked “increasing friction” (or interfacial shear stress) is clearly defined as such by the fringe behavior; in the domain marked “constant friction,” the fringe variations are consistent with this interpretation, but the implication is not as clear due to noise. A peak in the fringes on the specimen mid-plane locates the onset of unloading.

Figure 4 presents images similar to that in Fig. 3 but taken from experiments conducted with higher and lower static pre-loads. The difference in the visibility of bands in these figures and Fig. 3 is representative. Further inspection of Figs. 3 and 4 shows that as the pre-load increases, the kinking of the fringes is associated with larger distortions, suggesting that the onset of sliding is associated with a sharper discontinuity. A similar trend was observed as the impact speed was increased. The dynamic sliding process is associated with higher, more localized stresses at higher loading rates and higher static pre-load.

Sliding Speeds:

The velocity of the dominant band in each image along the interface was estimated by comparing its position in successive frames. Figure 5 shows plots of the positions of the intersections of a symmetric pair of such bands with the top and bottom interfaces as a function of time for an experiment conducted with 12.5 MPa pre-load and 38 m/s impact speed. The bands propagate at the same velocity on the top and bottom and the variation of sliding position with time is essentially linear. This contrasts with the common case for shear crack propagation, where a period of acceleration of the crack tip is often observed, which may approach constant velocity asymptotically. Here, the velocity of the bands is constant throughout the experiment, within the experimental error of approximately $\pm 3\%$ (typically on the order of ± 50 m/s). These observations were consistent in all of the experiments, indicating that on this scale of observation, sliding is a steady-state process. In this particular experiment, the slope of the plot in Fig. 5 indicates a sliding speed of 2050 m/s or approximately the dilatational wave speed of Homalite. Model analysis (see below) suggests that these bands probably corresponded to the beginning of a domain of enhanced interfacial shear stress.

Figure 6 provides a summary of the velocities of the dominant bands measured from all of the experiments, plotted as a function of static pre-load. While the data show substantial scatter, individual points are accurately determined (see above). In all cases, the observed speeds were in excess of the shear wave speed of Homalite, i.e., greater than 60% of the dilatational wave speed. In general, the trend is toward decreasing sliding speed with increasing static pre-load. However there is no clear functional dependence. Insight provided by modeling (see below) suggests that the bands identified as dominant in collating the data of Fig. 6 may have corresponded in some cases to the onset of interfacial sliding, but in other cases to the beginning of a domain of increasing interfacial shear stress.

Data for all of the experiments conducted at 0.5 MPa and varying impact speed lie along the ordinate (the axis of sliding speed) in Fig. 6. There was no systematic variation of sliding speed with impact speed, with all the measured sliding speeds being approximately the dilatational wave speed of Homalite.

Sliding Stresses and Loading Rate: The photoelastic fringes can be equated to the local difference in principal stresses:

$$\sigma_1 - \sigma_2 = F_\sigma N / W \quad (1)$$

where F_σ is the stress-optic coefficient (22.6 kN/m for Homalite), N is the fringe order, and W is the specimen width (in the through-thickness direction, x_3). The stress along the center-line of the Homalite can be determined from Eq. (1) alone if the following conditions are met: 1) the principal stresses along the center-line act in the x_1 and x_2 directions and; 2) plane stress conditions exist; and 3) strains ε_{22} in the x_2 direction are negligible. Then Eq. (1) reduces to

$$\sigma_1(1 - \nu) = F_\sigma N / h \quad (2)$$

where ν is Poisson's ratio for the Homalite; and hence the stress distribution along the center of the fiber can be determined. The condition of negligible strain component, ε_{22} , will not be met in the presence of large compressive pre-stress. Nevertheless, Eq. (2) proves useful, for the following reasons. First, numerical simulations (see below) show

that, in the absence of compressive pre-stress, dynamic contributions to ε_{22} are very small; and the stress, σ_1 , estimated from experiments using Eq. (2) and that calculated by the simulations are very close. Second, when the compressive pre-stress is large, the additional contribution to ε_{22} will be time-invariant. Therefore, Eq. (2) can be used to estimate the applied loading rate, $d\sigma_1/dx_1$, in steady-state conditions from experimental data, since this involves taking a derivative.

The variation of stress with position is found to be approximately linear, yielding a constant value of $d\sigma_1/dx_1$ for each test. (Thus experiments and simulations (see below) confirm the rapid attainment of steady-state conditions in the axial stress and the proper application of Eq. (2).) This steady-state value can be divided by the dilatational wave speed in Homalite to give a loading rate per unit time. The loading rate rises in proportion to the impact speed and decreases linearly with static pre-load (Fig. 7). When the coupling of the fiber and the matrix is increased, the input momentum is transferred more rapidly to the matrix, resulting in slower loading of the fiber.

3. Numerical Modeling

A computational simulation of the test was set up in a commercial finite element package (ABAQUS¹), with cohesive elements to represent interface friction. Symmetrical boundary conditions ($u_3 = 0$; $\tau_{12} = 0$) were imposed along the center of the Homalite piece ($x_2 = 0$) and the top surface of the steel piece. A state of plane stress was assumed in the (x_1, x_2) plane. Semi-infinite elements were used to prevent elastic waves bouncing back from the right end of the model (Fig. 8). The cohesive elements introduce a relationship between the shear tractions, τ_{int} , and the sliding displacement rate, $[\dot{u}_1]$, at the interface. The law used (Fig. 9) is intended to represent friction that is uniform and constant in magnitude, but an initial linear part is included to avoid numerical difficulties where the sense of the motion changes. A dynamic loading history (Fig. 10), corresponding to that caused by the experimental impactor, was imposed as a prescribed stress, $\sigma_{11}(t)$, acting uniformly over the interval $-h < x_2 < h$ at the left end of the Homalite. The simulation described in detail in the following had a loading rate, $d\sigma_{11}/dt = 31.5 \text{ MPa}/\mu\text{s}$, a rise time

¹ ABAQUS, Inc., Pawtucket, RI 02860

of 6.0 μs , and linear unloading over a further 12.0 μs . The loading rate and maximum stress correspond to those deduced from measurements of stress distributions at the end of the Homalite for the test with an impactor velocity of 39 m/s and a compressive pre-stress, $\sigma_{22}^{(r)} = 50$ MPa. The unloading rate was set to be half that of the loading rate in magnitude, which also corresponded approximately to the measured rate. Thus the boundary stress was not predicted, but fitted to experiments; but all other characteristics of the deformation, including front velocities and the general distribution of stresses, etc., were predicted given only this fitted condition. The interfacial frictional stress was assigned the magnitude $\tau_f = 40$ MPa. This would correspond to a friction coefficient of 0.8 for the same test, if friction had obeyed Coulomb's law in the test; but this, of course, may not have been the case. The magnitude of τ_f was held constant in the simulations. Since the loading rate depends only weakly on the compressive pre-stress (Fig. 7), the simulation could also be interpreted as representing cases of higher compressive pre-stress, if a lower value of the coefficient was believed to be more appropriate. (The calculation would be unchanged because the coefficient of friction does not enter explicitly into the model.)

3.1 General Character of the Predicted Wave Deformation

Figure 11 shows predicted contours of the principal stress difference $\sigma_1 - \sigma_2$ and the shear stress τ_{12} in the Homalite at time $t = 9.822$ μs . These plots and plots of stress variations along single lines (see below) distinguish four zones in the wave propagation. Right-most is the so-called head wave zone, where the interface friction stress is opposite in sense to that in the trailing zones. (This change of sign is not evident in Fig. 11b, because of the small magnitudes of the stresses involved.) In the head wave zone, the Homalite is loaded by the steel and the wave speed exceeds that of Homalite, C_f , by a factor of more than 2 (the factor being difficult to pinpoint numerically) but is less than that of the steel, C_m .

Following the head wave zone is a linearly increasing shear stress zone, where the interface (friction) stress increases approximately linearly with position up to the limiting value, τ_f , given by the cohesive law. This zone derives from the finite-sloped transition

from negative to positive shear stress used in the cohesive model to avoid numerical problems (Fig. 9). However, domains with this character were also observed in the model experiments, suggesting that the law of Fig. 9 may fortuitously represent, at least qualitatively, the true constitutive behaviour of the interface under rising shear stress. The next zone is the constant friction zone, which is characterized by a suddenly and greatly reduced density of the contours in σ_1 - σ_2 , while the shear stress is constant at the value, τ_f .

The last zone is associated with the unloading part of the loading history. The contour lines near the interface become chaotic, which is also seen in the experiments (Figs. 3 and 4). In the simulation, alternating contact and separation zones exist along the interface in this region. The experimental contours show similar variations, suggesting the same contact behaviour (although in the experiments no direct confirmation of interface displacements is possible).

4. Stress Distributions and Front Velocities

Comparison of the measured and predicted stress contours has shown that, even though the numerical model is based on an *ad hoc* and probably incorrect friction law, most aspects of the experiments appear to be reproduced. Further insight into the physics of the deformation is available from other calculated and measured characteristics.

Figures 12a – 12c show stress profiles at three different instants during the simulations of Fig. 11. Figure 12a shows the axial stress along the center line of the Homalite, $\sigma_{11}(x_1, 0)$, along with a measurement from the experiment executed with impactor velocity, $v_0 = 39$ m/s and compressive pre-stress, $\sigma_{22}^{(r)} = 50$ MPa. The agreement between the simulation and the experiment is quite close. (See also the discussion following Eq. (2).) The furthest disturbance evident in this plot corresponds to the transition in Fig. 11 from the head wave to the domain of linearly increasing friction. The peak axial stress along the center line decreases as the wave propagates, which is attributed to the dissipative frictional sliding process along the interface. Invariance of the stress profile confirms the

attainment of steady state conditions by time 6.2 μsec , shortly after peak load is attained at 6.0 μsec .

Figure 12b shows the interface shear stress at the same three instants. The shear stress increases approximately linearly until the constant friction stress assigned in the cohesive law is reached. It remains almost constant through the “constant friction” zone of Fig. 11, although small oscillations are evident around the prescribed value, τ_f . The unloading zone is dominated by high frequency, severe fluctuations in τ_{int} .

Figure 12c shows the axial stress, $\sigma_{11}(x_1, h)$, along the interface. A knee behind the furthest visible disturbance corresponds to the transition from linearly increasing to constant interfacial stress. In the region ahead of the knee, the loading rate of the material is remarkably small.

Figure 12d illustrates further the nature of the interface fields in the chaotic unloading zone. Large spikes in the fiber sliding displacement periodically reach down to the sliding displacement of the matrix, indicating locations of fiber/matrix stick. Reverse slip is also possible for brief intervals at these locations, but is difficult to resolve in a numerical simulation, due to computational noise.

The plots of Fig. 12 provide reasonably accurate information for evaluating the velocities of the various fronts. Fig. 13 shows histories of the locations of fronts as functions of time, obtained by interpolating measurements of the locations of the corresponding features in Fig. 12. The leading edge of the head wave is not shown, since it could not be accurately discerned.

The velocity, V_2 , of the transition to the linearly increasing friction zone is evaluated from both the earliest significant axial stress along the center line and the earliest significant shear stress along the interface. The former gives, $V_2 = 1.04C_f$, while the latter yields a slightly lower value $V_2 = 0.98C_f$. To within reasonable uncertainty, neither is significantly different from the wave speed in Homalite.

The front of the constant friction zone can only be determined accurately from the interface stresses, either the knee in the axial stress or the onset of the shear plateau (Fig.

12b). The inferred wave velocity is $V_3 = 0.87 \pm 0.02 C_f$, the error reflecting the difference between the two sources and the axial stress implying the higher value.

The front associated with the onset of unloading is best identified by the peak in the axial stress along the center line of the Homalite (Fig. 12c). The velocity takes the value $V_4 = 0.98 \pm .02 C_f$, once again close to the wave speed in the Homalite.

The velocity estimates can be approximately confirmed by analysing the bands or kinks in the predicted stress contours, which propagate from locations on the interface at which a transition (non-smooth behaviour) is present in the displacement fields. Two bands are traced by dashed lines in Fig. 11, emanating approximately from the fronts associated with the onset of linearly increasing friction and constant friction (sliding). The angles subtended by the lines to the interface, α_i , $i = 2$ and 3 , are given by $\sin \alpha_i = C_s/V_i$, where C_s is the shear wave speed in the Homalite. While difficulty arises in locating the bands on some contours, the fitted values $\sin \alpha_2 \approx 0.45$ and $\sin \alpha_3 \approx 0.6$ are probably correct to within 20%. These values yield $V_2 = (2.2 \pm 0.4)C_s$ and $V_3 = (1.6 \pm 0.3)C_s$, in reasonable agreement with the more accurate values deduced above from Fig. 12. The boundary of the domain of chaotic fields is also marked by a dashed line in Fig. 11, which emanates from the unloading front. The angle subtended by this line, $\alpha_4 \approx \arcsin 0.35$, yields $V_{\text{chaos}} = (3.0 \pm 0.3)C_s$. This high implied velocity is consistent with the observation in the simulations that the onset of chaos is delayed somewhat after the beginning of unloading, but the chaotic zone tends subsequently to catch up with the unloading front, and therefore propagates at a velocity exceeding that of the unloading front, or approximately C_f .

The different velocities predicted for the onset of sliding and the beginning of the domain of increasing interface shear help understand the distribution of the data in Fig. 6. Some uncertainty arose in identifying bands in fringe images (as described above), so that the nature of the interfacial phenomenon corresponding to a particular band was not always clear. Given the velocities predicted by the model, those data in Fig. 6 falling close to C_f would be associated with the beginning of the domain of rising interfacial shear stress, while other data would be associated with the sliding front.

Since the front of the constant friction zone propagates at slightly different velocities at the interface and along the center of the Homalite, the configuration of contours must change with time. Other contour plots at different times (not shown) show that the nearly parallel, vertical contours in the “linearly increasing friction” and “constant friction” zones of Fig. 11 do move apart more rapidly at the center of the Homalite than at the interfaces, which causes them to bow out towards the head wave with increasing time. The same fringe divergence was seen (via dynamic photoelasticity) in the model experiments. In both the simulations and the experiments, the divergence is limited in magnitude and the stress contours remain at angles less than approximately 10° from vertical during passage of the deformation along the length of the test piece.

Other changes with time are: 1) The zone of chaotic contours grows into the interior of the Homalite with time. In fact, other contour plots from the same simulations as reported in Fig. 11 reveal that chaotic behaviour does not appear at all until the elapse of approximately $8 \mu\text{s}$. 2) The constant friction stress zone shrinks with time, since $V_4 > V_3$, indicating that the unloading wave propagates faster than waves ahead of it.

5.0 Results from Shear Lag Models based on Lamé Fields

For the static problem of Fig. 1 and related thermal and mechanical problems, many useful results have been obtained using shear lag analysis and the assumption that the fiber deformation fields are separable in x and the transverse or radial variables; and that fields are simple, known functions of the latter (Cox, 1990; Cox *et al.*, 1990; Hutchinson and Jensen, 1990; Marshall *et al.*, 1985; McCartney, 1987). Analysis shows that these approximations give quite accurate predictions of the end load vs. the end displacement as long as the slip distance is long compared to the fiber diameter (or fiber width in a plane problem) (Hutchinson and Jensen, 1990). The fiber fields are well represented; and also the matrix fields, provided the volume fraction of fibers is not too small. Since these results in the static case are simple and have enlightened many aspects of the mechanics and engineering principles of designing fiber-reinforced materials, the question of their utility in the dynamic case is of interest.

For dynamic end loading that increases linearly in time and friction that is uniform and constant, shear lag analysis predicts that the deformation will propagate in two or three domains, depending on the value taken by the following three dimensionless parameters (Sridhar *et al.*, 2003):

$$k = \frac{\tau_f C_f}{h} \bigg/ \frac{d\sigma_0}{dt} \quad C = \frac{C_f}{C_m} \quad \phi = \frac{fE_f}{(1-f)E_m} \quad (4)$$

where f is the fiber volume fraction. The specimen of Fig. 2 and the simulations have lateral boundary conditions that are not periodic and therefore are not in strict correspondence with the shear lag model of Sridhar *et al.*, but correspondence can still be sought, using the dimensions of the specimen, by setting $f = 8.25/50.8 = 0.162$. The domains predicted by shear lag modeling consist of different interfacial conditions: slip, stick, and reverse slip. For the case of the simulations reported in the last section, $k = 0.317$, $C = 0.378$, and $\phi = 0.0043$. Shear lag modeling predicts, for these values, that the deformation during the linearly rising part of the loading will comprise a stick zone and a slip zone (see Appendix A). Furthermore, the interface friction stress in the stick zone is negative and has a very small magnitude, 0.036 MPa (see Eq. (A.6)). The sign is negative because the matrix (steel), having the higher wave speed, is pulling the fiber along in this zone. The magnitude is small because the volume fraction of the fiber is small, so that the stresses in the matrix remain small, the spatial derivative remains small, and therefore the friction stress remains small. For the case studied, the shear lag model predicts (Appendix A) that the head wave front will propagate at $V_1 = 2.6 C_f$.

A further prediction of the shear lag model is that, if the fiber volume fraction rises, then the interface shear stress in the head wave zone will exceed the friction stress in magnitude and reverse slip will occur (consider Fig. A.1 as the parameter ϕ rises). The head wave zone would no longer be a stick zone.

Figure 11 broadly confirms the predictions concerning the head wave zone. The zone is a stick zone (no slip), the interface shear stress is negative and very small in magnitude, and the front velocity, while not well determined, is consistent with the value $2.6 C_f$.

The zone of linearly increasing friction in Fig. 11 has no analogue in the shear lag results of Sridhar *et al.*, because in that particular modeling, the friction stress was assumed to change sign with reversing slip direction as a step function. The zone of linearly increasing friction in Fig. 11 arises from the linear friction stress regime at small displacements in the law of Fig. 9. The constant friction zone of Fig. 11 is equivalent to the slip zone in the shear lag model. The front of the constant friction zone is predicted in the shear lag model to propagate at $0.73 C_f$. This is less than the velocity, $V_3 = 0.87 C_f$, computed in the simulations of Fig. 11. An interesting question is whether the two models would agree in the predicted front velocity for higher fiber volume fractions, equivalent lateral boundary conditions, and as the linearly varying domain in the constitutive law of Fig. 9 shrinks in extent.

If it is assumed that the friction stress value used in the shear lag model would vary with compressive pre-stress according to Coulomb's law, then a prediction of the variation of front velocities with compressive pre-stress can be made. Two such predictions for the

velocity of the sliding front, V_3 , have been superimposed on Fig. 6. The rates of change of the friction stress correspond to assuming a coefficient of friction of 0.1 or 0.4. The trends of the curves are not inconsistent with the weakly defined declining trend in the data, especially when those data lying at C_f , which are believed to correspond to the front of increasing interfacial shear stress, are excluded.

6.0 Possible Chaotic Behaviour

The noisy behaviour appearing in the unloading zone in the simulations does not appear to a numerical artefact, but rather a consequence of the modeling assumptions and the physics of the problem. If it were due to Gibbs' phenomenon, i.e., numerical ringing at a near-discontinuity in the solution, it would not be confined to the vicinity of the interface (note, for example, the smoothness of the axial stress at the center-line of the Homalite, Fig. 12a); nor to the unloading zone, since non-smoothness of equal strength exists in the fields at other fronts (zone boundaries).

The noisy behaviour is not associated with Coulomb's law, since this was not the constitutive assumption of the model. In fact, the friction law assumed (Fig. 9), which contains no relation between the friction stress and the normal pressure, is simpler than that used in most studies of either stability or ill-posedness in problems of slip between half-spaces. For the same reason, the predicted phenomenon cannot be directly related to Poisson's effect, even though Poisson's ratio was nonzero in the simulations.

The fact that the noisy behaviour is confined to the unloading zone, while the deformation propagates smoothly at a range of speeds in other zones, has no obvious analogue in any prior studies of instability. The closest to a hint of similar behaviour is in incomplete and unpublished results for the shear lag modeling described by (Sridhar *et al.*, 2003). Attempts to trace solutions for linear unloading that follows linear loading lead to apparently complex patterns of the birth and death of slip, stick, and reverse-slip zones, as the unloading wave overtakes deformation of earlier origin. The possibility is suggested (but not yet thoroughly researched) that arbitrarily small changes in the loading history causing finite changes in the subsequent pattern of slip, stick, and reverse-slip zones. In the shear lag problem, the only possible source of instability or complexity is the strong nonlinearity associated with the change in sign of the friction stress when the direction of interfacial slip changes. While the analysis is incomplete, the suggestion of chaotic behaviour in the shear lag model provokes the speculation that the noisy behaviour seen during unloading in the experiments and the numerical simulations is also an example of chaos.

Shear lag modeling also highlights the role, in the possible generation of chaotic behaviour, of the coupling of wave motions between the fiber and the matrix. For a fiber

in a rigid matrix, where the fiber deformation is modified by interfacial friction tractions that depend only on its own motion, stable and well-behaved solutions can be mapped out systematically for quite complex loading and unloading histories, e.g., by the method of characteristics (Nikitin and Tyurekhodgaev, 1990). This method is not useful when the fiber motion is coupled to that of a matrix.

Numerical solution of the shear lag problem, e.g., numerical solving of difference equations subject to the constraint that displacement fields are Lamé-like, is not enlightening, because the rapid births and deaths of different zones are quickly obscured in numerical noise at the fronts.

The similarity of the predicted domains of chaotic behaviour and those measured in the model experiments is very eye-catching (Figs. 4 and 11), but the conditions assumed for the interface are unlikely to be the same in the two cases. In particular, the friction law of Fig. 9 is an idealization that is likely to be an oversimplification of the true friction behaviour in the experiments (although the experimental law is not known in detail). This suggests that the putative existence of chaotic behaviour is not especially sensitive to details of the friction law, but could be a consequence of unloading with any friction law that possesses the strong nonlinearity of sign reversal.

7.0 Conclusions

Comparing the characteristics of model planar experiments, numerical simulations, and shear lag modeling leads to the following inferences about the push-in problem of interest (Fig. 1), for a bi-linear sequence of loading and unloading.

1. The broad characteristics of the deformation in the fiber, exclusive of shock waves, can be predicted at least qualitatively by simple shear lag models, in which the displacements are reduced to Lamé fields. The shear lag solutions have the advantage of proposing clearly defined zones of different slip behaviour, which while present in both the experiments and the numerical simulations, are not so easily identified in them without prior knowledge. For engineering studies of dynamic deformation in composites reinforced by fibers, rods, or stitches, shear lag results will convey at least the trends of dynamic response at the macroscopic level. For example, the dynamic fiber end displacement is likely to be described quite well by shear lag theory, since those fine details of the push-in (or pullout) phenomenon that shear lag theory misses are unlikely to strongly influence an quantity such as the end displacement, which is derived from integrated strains.

2. For the given geometrical conditions and loading rate, shear lag modeling correctly predicts the system of stick followed by slip found in the numerical simulations and model experiments, even though the details of the assumed or actual friction laws are likely to be different in all three. One infers that the pattern of zones is mainly determined by the interplay of stress waves of different speeds in the fiber and the matrix and is fairly insensitive to the friction constitutive law.
3. The speeds of fronts (or the boundaries between zones) are fairly well predicted by shear lag modeling, but more consistent between the numerical simulations and the model experiments. Shear lag modeling could be expected to be a better approximation as the volume fraction of the fibers rises.
4. As far as shear lag theory is accurate, results found here for plane geometry should be equally applicable to axisymmetric conditions, which are a useful approximation to composites of cylindrical fibers.
5. The literature is replete with analyses of frictional sliding between half-spaces under uniform far-field velocity conditions. For that problem, the presence of ill-posedness, instability, pulse and crack-like slip systems, etc., depends strongly on the nature of the friction law (see Introduction). The present study considers non-uniform (time dependent) loading, which yields results that are not accounted for by the prior literature. Complex behaviour, which may be chaotic, arises during unloading, but not at other stages of the deformation, in both the experiments and the numerical solutions. This behaviour appears to be a consequence of the strong nonlinearity associated with the sign reversal in the frictional tractions with slip direction and is not sensitive to the details of the friction constitutive law.
6. The results that some characteristics of engineering relevance, especially the fiber end displacement and the pattern and velocity of sliding fronts, are insensitive to details of the friction law (being so similar in the experiments, numerical modeling, and shear lag analysis) also contrasts with the literature on shear crack propagation. One would expect that as the frictional traction rises in magnitude, or a large debond energy is included in the problem, the fiber push-in problem would begin to manifest the complex dependence seen for shear cracks. At the same time, the conditions required for shear lag analysis to be accurate would be lost.
7. Changing the compressive contact pressure in the experiments has quantitative but not qualitative effect on the deformation patterns.

ACKNOWLEDGMENTS: QDY and BNC are grateful for support from the U.S. Army Research Office through contract number DAAD19-99-C-0042, administered by Dr. David Stepp.

References

- Adams, G.G., 1998. Steady Sliding of Two Elastic Half-Spaces with Friction Reduction due to Interface Stick-Slip. *Journal of Applied Mechanics* 65, 470-475.
- Andrews, D.J., 1976. Rupture velocity of plane strain shear cracks. *Journal of Geophysical Research* 81(32), 5679-5687.
- Bao, G., Suo, Z., 1992. Remarks on crack-bridging concepts. *Applied Mechanics Review* 24, 355-366.
- Broberg, K.B., 1994. Intersonic bilateral slip. *Geophys. J. Int.* 119, 706-714.
- Budiansky, B., Hutchinson, J.W., Evans, A.G., 1986. Matrix fracture in fiber reinforced ceramics. *Journal of the Mechanics and Physics of Solids* 34(2), 167-189.
- Burridge, R., 1973. *Geophysical Journal of the Royal Astronomical Society* 35, 439.
- Burridge, R., Conn, G., Freund, L.B., 1979. The stability of a rapid mode II shear crack with finite cohesive tractions. *Journal of Geophysical Research* 85, 2210-2222.
- Cochard, A., Rice, J.R., 2000. Fault Rupture Between Dissimilar Materials: Ill-Posedness, Regularization, and Slip-Pulse Response. *Journal of Geophysical Research* 105, 25891-25907.
- Cox, B.N., 1990. Interfacial sliding near a free surface in a fibrous or layered composite during thermal cycling. *Acta Metallurgica et Materialia* 38, 2411-2424.
- Cox, B.N., Dadkhah, M.S., James, M.R., Marshall, D.B., Morris, W.L., Shaw, M.C., 1990. On determining temperature dependent interfacial shear properties and bulk residual stresses in fibrous composites. *Acta Metallurgica et Materialia* 38, 2425-2433.
- Cox, B.N., Marshall, D.B., 1994. Concepts for bridged cracks in fracture and fatigue. *Acta Metallurgica et Materialia* 42(2), 341-363.
- Cox, B.N., Sridhar, N., 2001. Universal bridging laws for cracks in creeping media. *Advances in Fracture Research, Proc. Int. Conf. on Fracture, ICF10, Honolulu: Elsevier, Oxford.*
- Cox, B.N., Sridhar, N., Beyerlein, I., 2001. Inertial Effects in the Pullout Mechanism During Dynamic Loading of a Bridged Crack. *Acta Materialia* 49, 3863-77.
- Gao, H., Huang, Y., Abraham, F.F., 2001. Continuum and Atomistic Studies of Intersonic Crack Propagation. *Journal of the Mechanics and Physics of Solids* 49, 2113-2132.

- Hutchinson, J.W., Jensen, H.M., 1990. Models of fiber debonding and pullout in brittle composites with friction. *Mechanics of Materials* 9, 139-163.
- Lapusta, N., Rice, J.R., 2003. Nucleation and early seismic propagation of small and large events in a crustal earthquake model. *Journal of Geophysical Research* 108, doi:10.1029/2001JB000793.
- Marshall, D.B., Cox, B.N., Evans, A.G., 1985. The Mechanics of Matrix Cracking in Brittle-Matrix Fiber Composites. *Acta Metallurgica* 33(11), 2013-2021.
- Marshall, D.B., 1992. Analysis of fiber debonding and sliding experiments in brittle matrix composites. *Acta Metallurgica* 40(3), 427-441.
- Massabò, R., Cox, B.N., 1999. Concepts for bridged mode II delamination cracks. *Journal of the Mechanics and Physics of Solids* 47, 1265-1300.
- McCartney, L.N., 1987. Mechanics of Matrix Cracking in Brittle-Matrix Fibre-Reinforced Composites. *Proceedings of the Royal Society, London A* 409, 329-350.
- Needleman, A., 1999. An analysis of intersonic crack growth under shear loading. *Journal of Applied Mechanics* 66, 847-857.
- Needleman, A., Rosakis, A.J., 1999. The effect of bond strength and loading rate on the conditions of governing the attainment of intersonic crack growth along interfaces. *Journal of the Mechanics and Physics of Solids* 47, 2411-2445.
- Nikitin, L.V., Tyurekhodgaev, A.N., 1990. Wave Propagation and Vibration of Elastic Rods with Interfacial Frictional Slip. *Wave Motion* 12, 513-526.
- Prakash, V., Clifton, R.J., 1993. Time Resolved Dynamic Friction Measurements in Pressure-Shear. In: *Experimental Techniques in the Dynamics of Deformable Solids: Applied Mechanics Division*, ASME, pp. 33-48.
- Prakash, V., 1998. Frictional response of sliding interfaces subjected to time varying normal pressures. *Journal of Tribology* 120, 97-102.
- Ranjith, K., Rice, J.R., 2001. Slip Dynamics at an Interface Between Dissimilar Materials. *Journal of the Mechanics and Physics of Solids* 49, 341-361.
- Rosakis, A.J., Samudrala, O., Coker, D., 1999. Cracks Faster than the Shear Wave Speed. *Science* 284, 1337-1340.
- Sridhar, N., Yang, Q.D., Cox, B.N., 2003. Slip, Stick and Reverse Slip Characteristics during Dynamic Fiber Pullout. *Journal of the Mechanics and Physics of Solids* 51(7), 1215-1241.

Weertman, J.J., 1980. Unstable slippage across a fault that separates elastic media of different elastic constants. *Journal of Geophysical Research* 85, 1455-1461.

Xia, K., Rosakis, A.J., Kanamori, H., 2004. Laboratory Earthquakes: The Sub-Rayleigh-to-Supershear Rupture Transition. *Science* 303, 1859-1861.

Zheng, G., Rice, J.R., 1998. Conditions under which velocity-weakening friction allows a self-healing versus cracklike mode of rupture. *Bulletin of the Seismological Society of America* 88, 1466-1483.

Appendix — results from shear lag analysis

The following results are reproduced from (Sridhar *et al.*, 2003) and apply to the fiber/matrix geometry of Fig. 1 when friction is uniform and constant and the fiber is subjected to a linearly increasing end load. For this problem, three cases arise in the solutions, viz., cases where domains of slip occur, cases where domains of slip and stick occur, and cases where domains of slip and reverse slip occur. Figure A.1 shows how which of these cases prevails depends on the loading rate and material parameters of the problem. The parameter

$$k = \frac{\tau_f c_f}{h} \bigg/ \frac{d\sigma_0}{dt} \quad (\text{A.1})$$

represents the loading rate, with c_f the longitudinal wave speed in the fiber (Homalite), τ_f the constant friction stress, and $d\sigma_0/dt$ the rate of increase of the stress at the fiber end. With the subscripts f and m referring to the fiber and matrix, respectively, the parameters C and ϕ are defined by

$$C^2 = \frac{c_f^2}{c_m^2} = \frac{\hat{E}_f / \rho_f}{\hat{E}_m / \rho_m} \quad (\text{A.2})$$

$$\phi = \frac{f E_f}{(1-f) E_m} \quad (\text{A.3})$$

with $\hat{E}_i = E_i(1 - \mu_i)/((1 + \mu_i)(1 - 2\mu_i))$, $i = m$ or f , and E_i , μ_i , and ρ_i , $i = m$ or f , denoting Young's modulus, Poisson's ratio, and the density.

The case of the test shown in Figs. 3, 10, and 11, i.e., for 38 m/s impact speed, falls into the regime of stick/slip in the map of Fig. A.1. The front of the stick zone advances at a speed V_1 given by

$$V_1 = c_f \sqrt{\frac{1 + \phi}{C^2 + \phi}} \quad (\text{A.4})$$

while the front at which slip begins advances at a speed V_3 given by the root of a cubic equation in $\eta_3 = V_3/c_f$:

$$(\eta_3^2 + 2k\eta_3 - 1)(1 + C^2\eta_3\eta_1) + 2k\phi(1 + \eta_3\eta_1)\eta_3 = 0 \quad (\text{A.5})$$

Analysis shows that η_3 has only one real positive root which always lies in (0,1), whereas η_1 can clearly exceed unity. The interfacial friction stress in the stick zone is:

$$\tau = \tau_f \frac{(\eta_3^2 + 2k\eta_3 - 1)(1 - C^2)}{2k \left\{ \eta_3(1 - C^2) + (1 - \eta_3^2)\sqrt{(C^2 + \varphi)(1 + \varphi)} \right\}} \quad (\text{A.6})$$

where η_3 has been obtained by solving Eqn. (A.5). This expression for the friction stress always satisfies $|\tau| < |\tau_f|$.

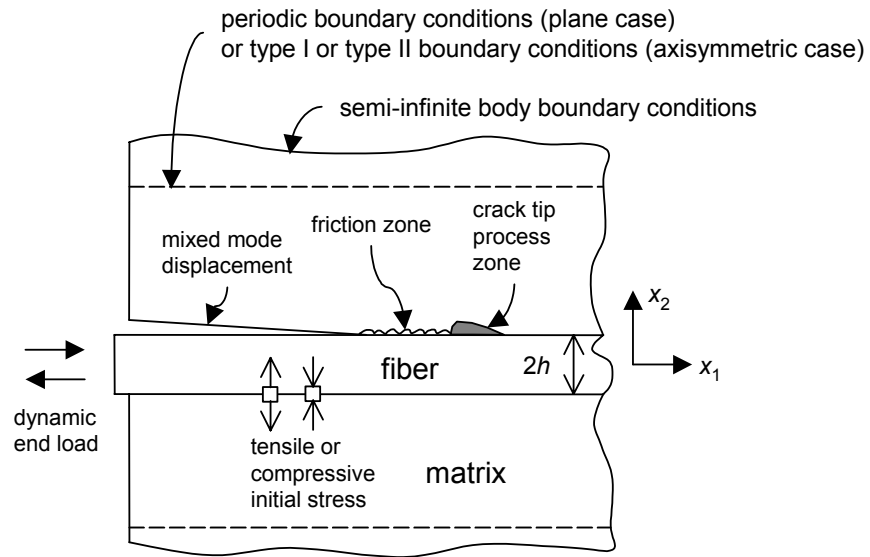


Figure 1. Schematic of a general problem of fiber/matrix debonding, under dynamic end loading, with possible crack wake friction.

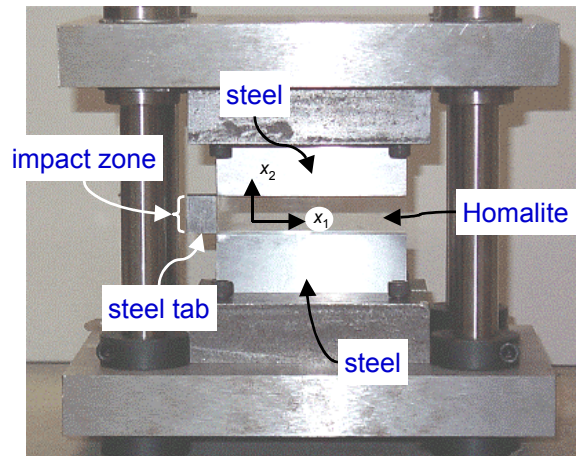


Figure 2: Planar test specimen under static pre-load applied to the top and bottom plates of the fixture.

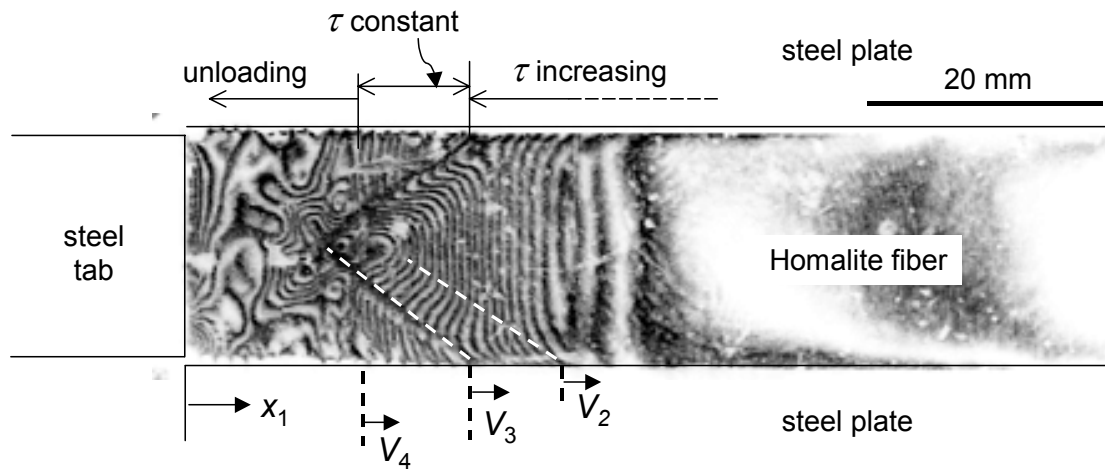


Figure 3. Representative image from a dynamic sliding experiment (38 m/s impact speed, 50 MPa static pre-load). (The constancy of the interface shear stress in the region labeled “ τ constant” is consistent with the fringe pattern, but not well resolved experimentally above the noise. It is marked so because of modeling results. The labels of the other domains are clearly implied by the nature fringe patterns.)

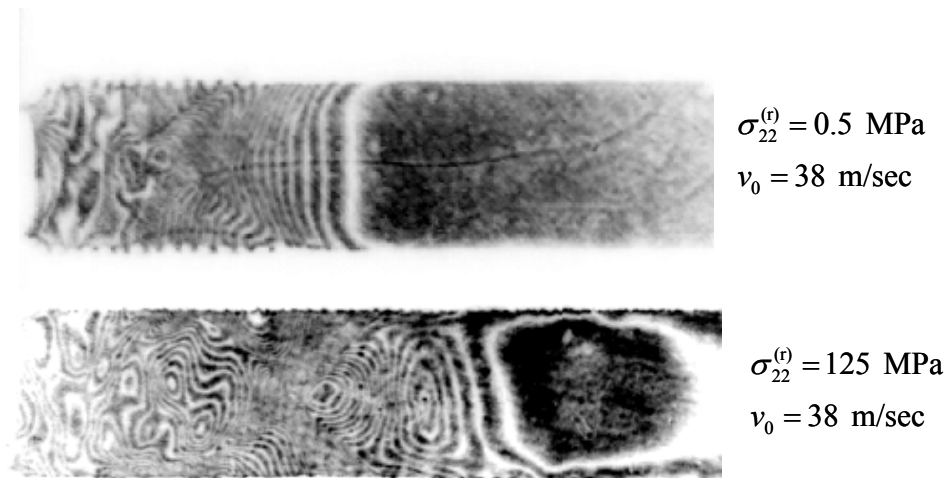


Figure 4. Fringe patterns obtained at low and high values of the static pre-load (as marked).

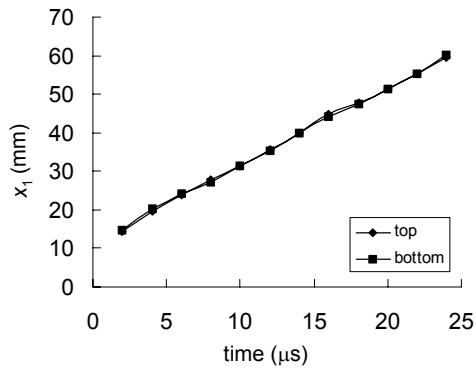


Figure 5: A plot of the location of sliding onset vs. time for a specimen impacted at 40 m/s with a static pre-load of 12.5 MPa.

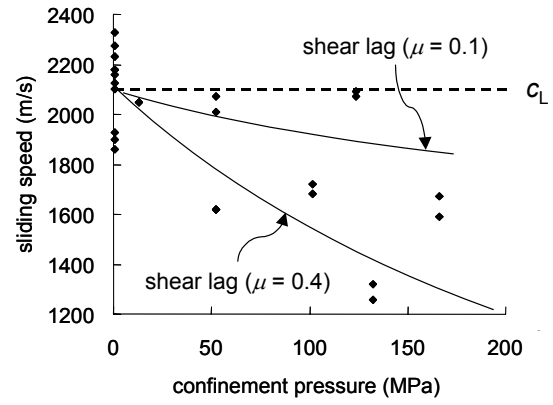


Figure 6: A plot of the variation of the speed of the sliding front with static pre-load.

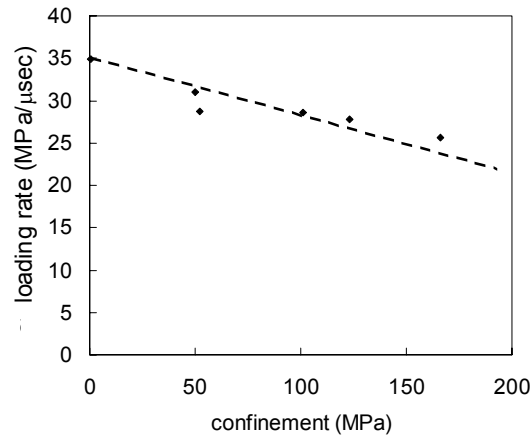


Figure 7: Variation of loading rate with magnitude of static compressive pre-load.

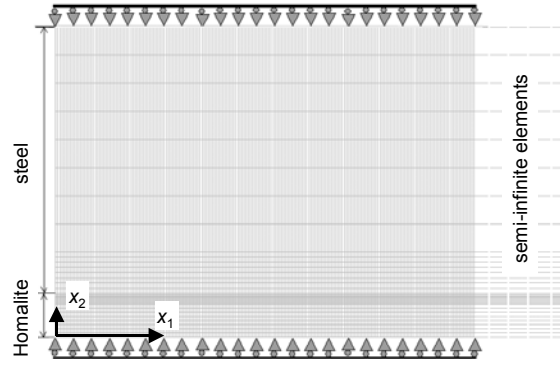


Figure 8: Mesh for numerical simulations.

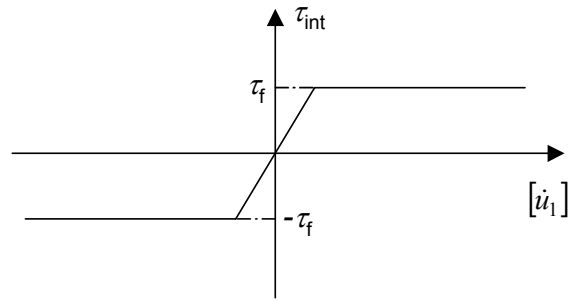


Figure 9: Interface friction law introduced via cohesive elements.

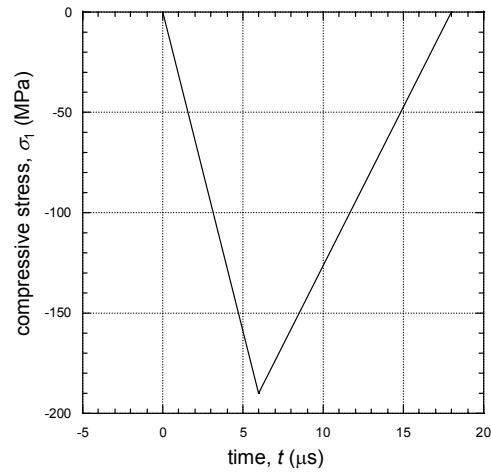


Figure 10. Loading history in simulation.

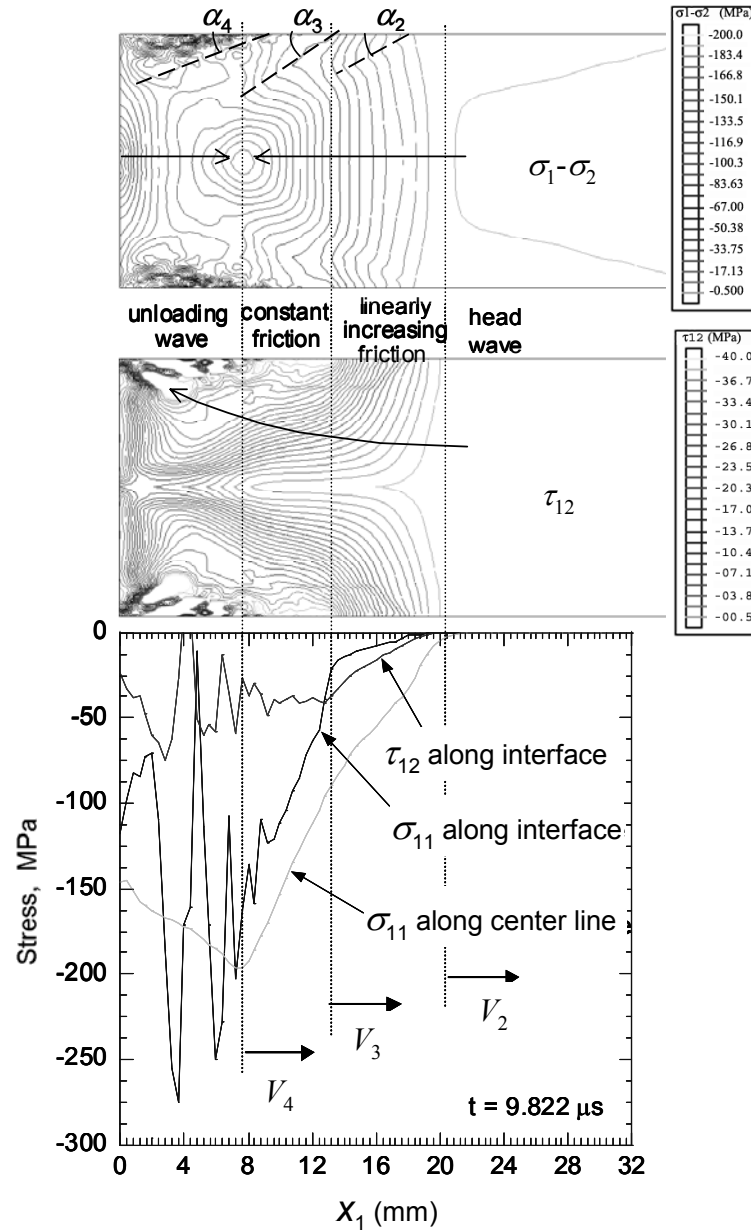


Figure 11: Calculated contour plots for $\sigma_1 - \sigma_2$ and τ_{12} in the Homalite at $t = 9.822 \mu\text{s}$. Arrows indicate direction of increasing magnitude of stress.

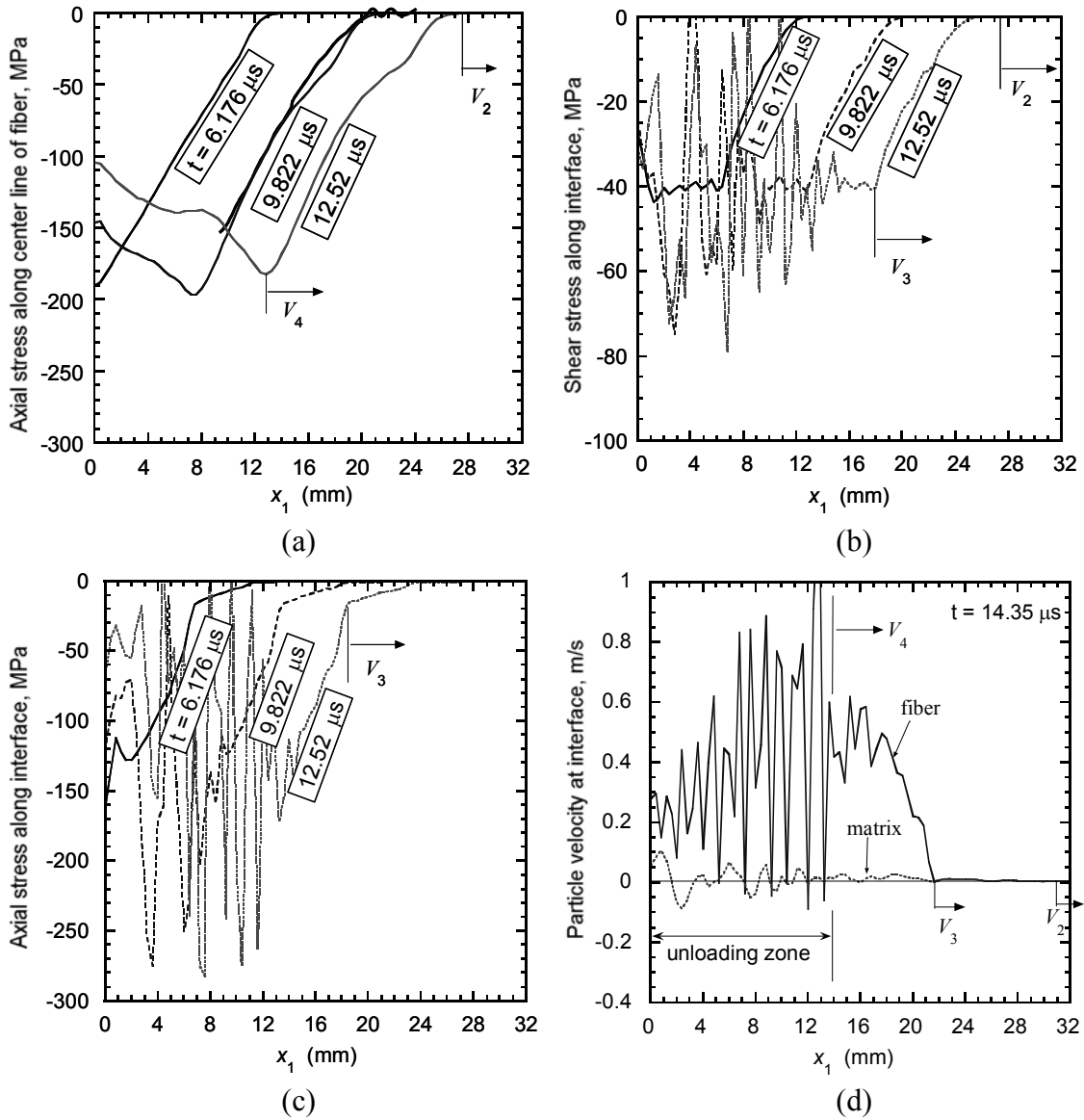


Figure 12. Stress and displacement profiles from numerical simulations. (a) axial stress, σ_{11} , along the center line of Homalite (heavy curve is experimental data); (b) shear stress, τ_{12} ; (c) axial stress, σ_{11} , along the interface; and (d) axial particle velocity in the Homalite (fiber) and steel (matrix) along the interface.

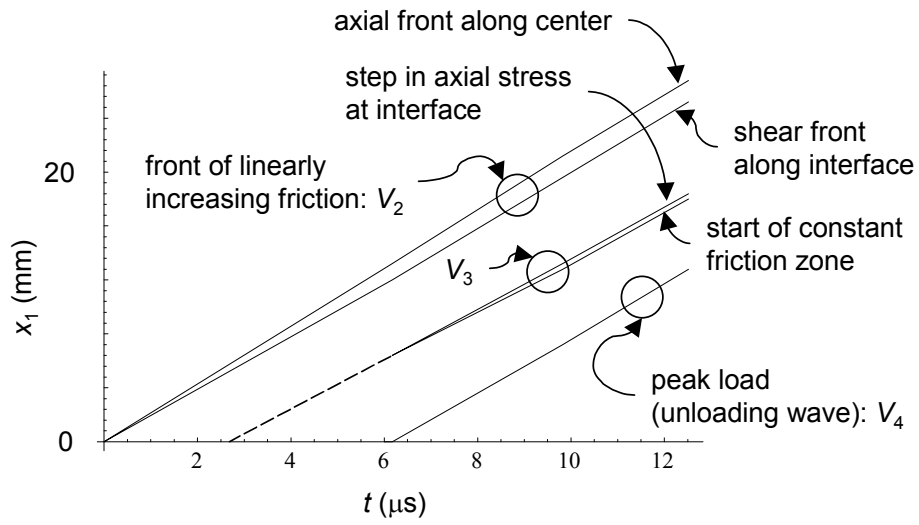


Figure 13. Front motions.

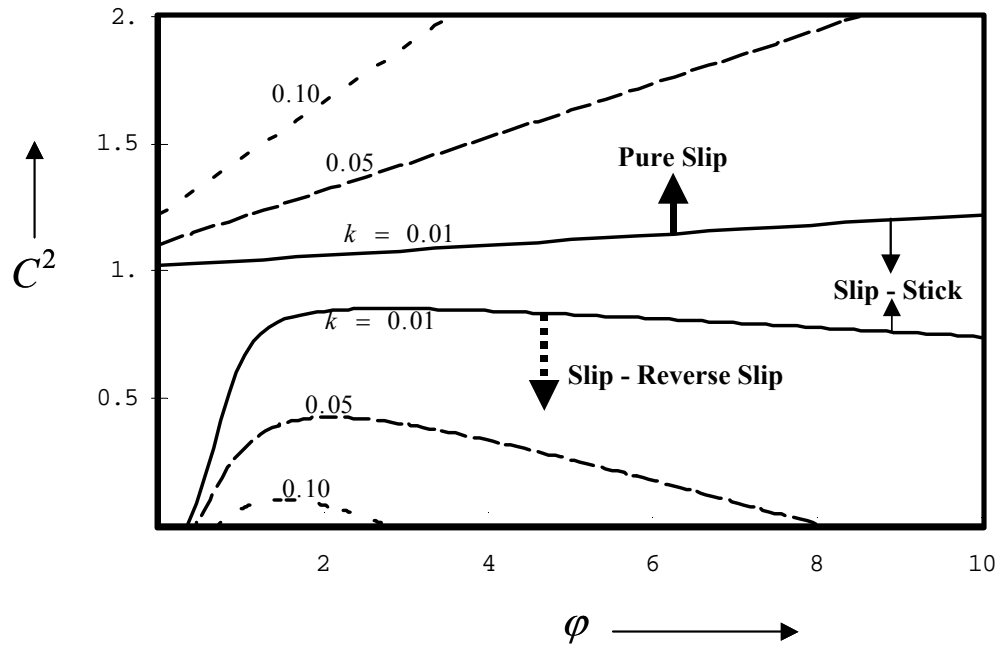


Fig. A.1. Domains in which different configurations of slip, stick, and reverse slip are predicted by shear lag analysis for a fiber push-in problem with constant loading rate